# The European Fault-Source Model 2020 (EFSM20): geologic input data for the European Seismic Hazard Model 2020

Roberto Basili[1], Laurentiu Danciu[2], Céline Beauval[3], Karin Sesetyan[4], Susana Pires Vilanova[5], Shota Adamia[6], Pierre Arroucau[7], Jure Atanackov[8], Stéphane Baize[9], Carolina Canora[10], Riccardo Caputo[11], Michele Matteo Cosimo Carafa[1], Edward Marc Cushing[9], Susana Custódio[12], Mine Betul Demircioglu Tumsa[13], João C. Duarte[12], Athanassios Ganas[14], Julián García-Mayordomo[15], Laura Gómez de la Peña[16], Eulàlia Gràcia[16], Petra Jamšek Rupnik[8], Hervé Jomard[9], Vanja Kastelic[1], Francesco Emanuele Maesano[1], Raquel Martín-Banda[15], Sara Martínez-Loriente[16], Marta Neres[17,12], Hector Perea[16], Barbara Šket Motnikar[18], Mara Monica Tiberti[1], Nino Tsereteli[6], Varvara Tsironi[14], Roberto Vallone[1], Kris Vanneste[19], Polona Zupančič[18], Domenico Giardini[20]

[1]Istituto Nazionale di Geofisica e Vulcanologia, Roma, 00143, Italy

[2]Swiss Seismological Service, ETH Zurich, Zurich, Switzerland

[3]ISTerre, IRD, Univ. Grenoble Alpes, Univ. Savoie Mont Blanc, CNRS, Univ. Gustave Eiffel, Grenoble, France

[4]Boğaziçi University, Kandilli Observatory and Earthquake Research Institute, Department of Earthquake Engineering, Istanbul, 34684, Turkey

[5]Instituto Superior Tecnico, Universidade de Lisboa, Lisbon, Portugal

[6]Institute of Geophysics, Ivane Javakhishvili Tbilisi State University, Tbilisi, Georgia

[7]Electricité de France, TEGG, Aix-en-Provence, France

[8]Geological Survey of Slovenia, Ljubljana, Slovenia

[9]Institut de Radioprotection et de Sûreté Nucléaire, Fontenay-aux-Roses, France

[10]Universidad Autónoma de Madrid, Facultad de Ciencias. Dpto. Geología y Geoquímica, Madrid, 28049, Spain

[11]Department of Physics and Earth Sciences, University of Ferrara, Ferrara, Italy

[12]Instituto Dom Luiz (IDL), Faculdade de Ciências, Universidade de Lisboa, Lisbon, 1749-016, Portugal

[13]Turkish Earthquake Foundation, Istanbul, Turkey

[14]National Observatory of Athens (NOA), Athens, Greece

[15]Instituto Geológico y Minero de España (IGME-CSIC), Madrid, 28760, Spain

[16]Institut de Ciències del Mar-CSIC, Barcelona, Spain

[17]Instituto Português do Mar e da Atmosfera, 1749-077 Lisboa, Portugal

[18]Slovenian Environment Agency, Ljubljana, Slovenia

[19]Royal Observatory of Belgium, Brussels, Belgium

[20]Institute of Geophysics, Dep. of Earth Sciences, ETH Zurich, Zürich, Switzerland

*Correspondence to*: Roberto Basili (roberto.basili@ingv.it)

**Abstract.**

Earthquake hazard analyses rely on seismogenic source models. These are designed in various fashions, such as point sources or area sources, but the most effective is the three-dimensional representation of geological faults. We here refer to such models as fault sources. This study presents the European Fault-Source Model 2020 (EFSM20), which was one of the primary input datasets of the recently released European Seismic Hazard Model 2020. The EFSM20 compilation was entirely based on reusable data from existing active fault regional compilations that were first blended and harmonized and then augmented by a set of derived parameters. These additional parameters were devised to enable users to formulate earthquake rate forecasts based on a seismic-moment balancing approach. EFSM20 considers two main categories of seismogenic faults: crustal faults and subduction systems, which include the subduction interface and intraslab faults. The compiled dataset covers an area from the Mid-Atlantic Ridge to the Caucasus and from northern Africa to Iceland. It includes 1,248 crustal faults spanning a total length of ~95,100 km and four subduction systems, namely the Gibraltar, Calabrian, Hellenic, and Cyprus Arcs, for a total length of ~2,120 km. The model focuses on an area encompassing a buffer of 300 km around all European countries (except for Overseas Countries and Territories) and a maximum of 300 km depth for the subducting slabs. All the parameters required to develop a seismic source model for earthquake hazard analysis were determined for crustal faults and subduction systems. A statistical distribution of relevant seismotectonic parameters, such as faulting mechanisms, slip rates, moment rates, and prospective maximum magnitudes, is presented and discussed to address unsettled points in view of future updates and improvements. The dataset, identified by the DOI https://doi.org/10.13127/efsm20, is distributed as machine-readable files using open standards (Open Geospatial Consortium).

## 1 Introduction

Seismogenic fault-source models are mathematical representations of the characteristics and behavior of earthquake faults. They are used to simulate how earthquakes might occur in any given region and to estimate the expected ground shaking intensity. Fault-source models can also be used to simulate earthquake-triggered tsunamis, ground-surface displacement, and various secondary effects (e.g., landslides, liquefactions). Considering that seismic sources in earthquake hazard studies are modeled in different fashions, such as point or area sources, we here refer to a fault source to designate the geological fault capable of being reactivated and generating earthquakes.

In this context, geological and paleo-seismological data provide a framework to estimate the average long-term recurrence time of possible earthquakes on known faults. These earthquakes often have recurrence intervals that are longer than instrumental and historic seismic catalogs, so geologic-fault information can effectively complement the recurrence statistics of earthquake catalogs where they lack more data. The combination of the spatial scale in fault mapping and the temporal scale of their recurrent behavior in generating earthquakes makes the geologic fault data more important, relative to other datasets, in forecasting larger magnitude earthquakes.

This work documents the European Fault-Source Model 2020, EFSM20 (Basili et al., 2022), a data product of the EU H2020 Project SERA (WP25-JRA3), designed to fulfill the requirements related to active faulting of the 2020 update of the European Seismic Hazard Model, ESHM20 (Danciu et al., 2021, 2022), following the probabilistic framework established for the 2013 European Seismic Hazard Model, ESHM13 (Woessner et al., 2015). To this end, the model aimed to cover a target area for foreseen ground motion that encompasses a buffer of 300 km around all European countries except for Overseas Countries and Territories (OCTs). The 300 km value estimate comes from the distance at which the ground motion propagated from a given source becomes negligible at the target site, based on ESHM13 ground motion model selection and outcomes (Delavaud et al., 2012; Woessner et al., 2015). We extend this concept also to the depth direction for deep earthquakes. The model, however, extends beyond this area to gain insights from the good continuity of plate boundaries.

We defined two fault-source categories: crustal faults and subduction systems. A crustal fault is a fracture or a system of fractures that separates different blocks of the Earth's crust. This category includes faults in various tectonic contexts, including onshore and offshore active plate margins and interiors. A subduction system is a combination of structures formed where one plate (the slab) moves under another (the upper plate) and sinks into the mantle beneath it. This process results in a convergent movement of the two involved plates, which is known to generate earthquake ruptures of different types (Satake and Tanioka, 1999). This category includes the detachment at the base of the accretionary wedge, the interface between the two plates at crustal depth, and the dipping slab at mantle depth. These three elements are all part of the lower plate. The possible splay faults, branching upward into the upper plate from the subduction interface, are included in the crustal faults category.

The EFSM20 compilation is entirely based on published reusable data. Details about these data and how they were used are given in Sections 2 and 3. We then performed data curation and harmonization (i.e., treating the complementary compartments of the different datasets to have them working together) to provide the user with all the necessary elements to develop a seismic source model and, ultimately, build an earthquake rate forecast. Although EFSM20 was designed for developing earthquake hazard models, it can also assist post-earthquake analyses and tectonic or geodynamic modeling.

The EFSM20 dataset includes 1,248 crustal faults spanning a total length of ~95,100 km – with an individual end-to-end length range of ~4-900 km - and four subduction systems, namely Gibraltar, Calabrian, Hellenic, and Cyprus Arcs, spanning a total length of ~2,120 km – with an individual end-to-end length range of ~220-1010 km (Figure 1). The dataset distribution includes several layers providing different map feature implementations linked to relevant parameters. Such data layers are made available through the European Databases of Seismogenic Faults portal with a dedicated webpage (https://seismofaults.eu/efsm20) that directs the users to Open Geospatial Consortium (OGC; https://www.ogc.org/) web services (WFS and WMS), downloadable GIS files in various formats (GeoJSON, ESRI shapefile, MapInfo tables). The dataset files, web services, structure, and description of all fault-source attributes in tabular form are shown in Appendix A. EFSM20 is part of the EPOS TCS Seismology EFEHR portfolio (Haslinger et al., 2022) and is already accessible through the EPOS Integrated Core Services data portal (https://www.ics-c.epos-eu.org/). The geographic distribution and comparison of the derived parameters most related to the seismogenic process, such as fault type, slip rate, moment rate, and maximum magnitude, are discussed in Section 4.

Although the continent scale of the collection prevented us from exploring each fault in great detail, and several fault parameters are affected by significant approximations, EFSM20 covers the major plate boundaries around the European plates and their interiors. The machine-readable fault attributes allow users to develop earthquake rate forecasts straightforwardly, promoting future updates to address unsettled points and meta-analyses and curiosity-driven studies to enhance our understanding of the seismogenic processes.
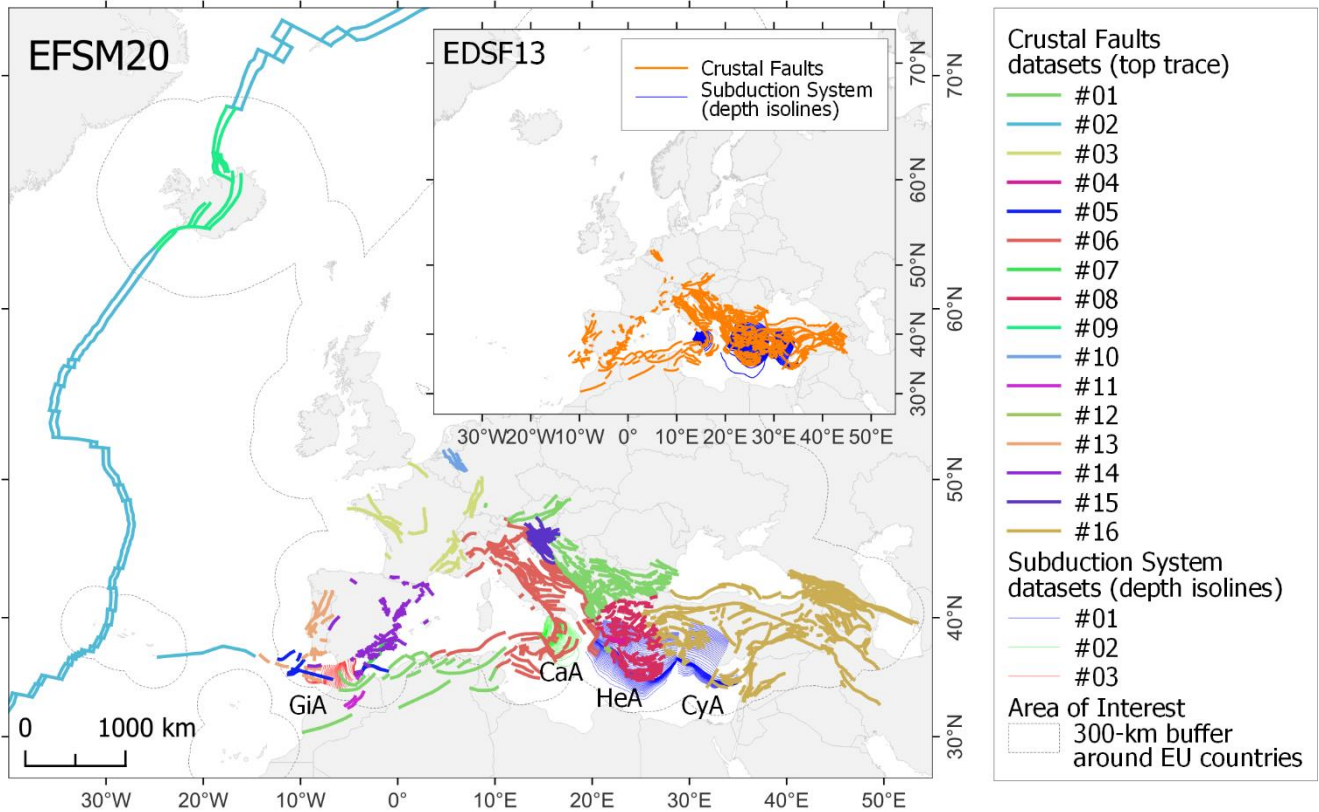
**Figure 1: Map of collated fault datasets for developing the European Fault-Source Model 2020 (EFSM20). The colors in the legend identify the various datasets (see Section 3 for their descriptions). From west to east, the subduction systems are Gibraltar Arc (GiA); Calabrian Arc (CaA); Hellenic Arc (HeA); and Cyprus Arc (CyA). The Inset map shows the European Database of Seismogenic Faults 2013 (EDSF13) for comparison.**

## 2 Data and Methods

The EFSM20 compilation was entirely based on reusable data. We started the initial collection from the Pan-European compilation EDSF13 (Basili et al., 2013) and progressively replaced it with up-to-date regional datasets.

We considered primarily the compilations that covered with a consistent approach significantly large regions, relying on the work of the authors of each compilation regarding the accuracy and recency of the information. We resorted to using smaller-

scale studies only in case of undefined situations, e.g., area of overlap between two regional datasets or cases where a significant update was available or where the fault information was not covered by the initial pan-European dataset but deemed necessary. Regardless of size and coverage, all considered datasets must comply with a series of requirements. Each crustal fault must have been declared active under one of the many existing definitions by the dataset authors or contributors. On the one hand, reviewing the definition of active fault was beyond the scope of this work. On the other hand, we recall that the definition of active faults may even differ in different tectonic settings. Subduction systems, instead, are included in the compilation regardless of the activity definition. The minimum set of basic fault parameters required for constructing a seismogenic source model refers to geometry (location: latitude, longitude, depth; size: length, width; orientation: strike, dip) and behavior (rake and slip rate). These are indispensable elements for devising and applying a fault recurrence model to be expressed by a Frequency-Magnitude Distribution (FMD). Not all fault compilations fully provide this characterization, and strategies were devised to fill in the missing information and harmonize it.

We assigned a unique identifier (ID) to each retained record in the collated dataset to avoid possible ambiguities in identifying the faults. The ID is a 7-character string, in which the first two positions are occupied by the letters "CF" for crustal faults and "SS" for subduction systems, followed by the standard ISO 3166 2-letter code, which identifies the country where most of the fault is located, followed by an alphanumeric 3-letter code (e.g., CFCH0B5 identifies the crustal fault 0B5 which is in Switzerland). To track the provenance of each record, we assigned an identifier to the original dataset and stored the original fault identifier in that dataset. See Appendix A for a complete description of all fault parameters.

The next subsections summarize the main adopted datasets (Figure 1; each record in EFSM20 reports its provenance to one of them) and describe the procedures to retrieve the initial geometry and relevant parameters, as well as the additional data used to harmonize the collation and estimate the derived parameters. Crustal faults and subduction systems are treated separately.

## 2.1 Crustal-fault datasets

Dataset #01: This is the original database EDSF13, compiled in the framework of the SHARE project (Basili et al., 2013), which covered Europe and the Mediterranean region. This dataset was adopted as the starting point to build the new crustal fault-source model. The largest regions that remained unmodified are the Balkans and northern Africa. According to individual studies, most regions were entirely replaced by new datasets or partly revisited. Elements added in regions that EDSF13 did not cover are in Iceland, France, and the northern Mid-Atlantic plate boundary. The major regional updates are summarized below.

Dataset #02: This dataset covers the Mid-Atlantic ridge and transforms. The initial geometry was derived from a global plate-boundary model (Bird, 2003), and the rest of the characterization was based on the oceanic crust age and spreading rate (Müller et al., 2008). For the transform faults, the slip rate was directly derived from the spreading rate, aided by more local data for the Gloria fault (Fadil et al., 2006; Koulali et al., 2011). For the normal faults, the slip rate was obtained by combining the spreading rate with local information about fault spacing and heave (MacDonald and Luyendyk, 1977; Escartín et al., 1999).

Dataset #03: This dataset covers the French region and is derived from BDFA (Jomard et al., 2017). Due to the different strategies of fault mapping used in BDFA, we redrew the fault traces by interpolation and reassigned some parameters, particularly slip rates, based on recent regional works.

Dataset #04: This dataset includes a few faults in the Gulf of Corinth. The initial geometry of the faults is based on GreDaSS (Caputo and Pavlides, 2013), and the slip rates were updated based on recent works not included in the GreDaSS compilation (Bell et al., 2009; Fernández-Blanco et al., 2019).

Dataset #05: This dataset covers the offshore parts of the Gulf of Cadiz and the Alboran Sea. In this area, we updated the EDSF13 based on several recent works, providing updated geometries and/or slip rates (Koulali et al., 2011; Martínez-Loriente et al., 2018; Martínez-Loriente et al., 2013; Neres et al., 2016; Perea et al., 2018; Gómez de la Peña et al., 2018).

Dataset #06: This dataset covers the Italian territory and some surrounding regions. It is mainly based on the most recent version of the DISS (Basili et al., 2008; DISS Working Group, 2021).

Dataset #07: This dataset includes a few faults in the Eastern Betic region. Such faults represent modifications of QAFI (see Dataset #14) according to recent works with substantial updates of fault geometries and slip rates (Borque et al., 2019; Gómez-Novell et al., 2020a, b; Herrero-Barbero et al., 2020).

Dataset #08: This dataset covers the Aegean region. It is mainly based on the most recent version of GreDaSS (Caputo and Pavlides, 2013).

Dataset #09: In Iceland, we started from the same approach as the Mid-Atlantic ridge and transform faults (see Dataset #02) and added data and considerations based on local studies (Bergerat et al., 1990; Forslund and Gudmundsson, 1991; Rögnvaldsson et al., 1998; Garcia et al., 2002; LaFemina et al., 2005; Árnadóttir et al., 2008; Rust and Whitworth, 2019).

Dataset #10: This dataset deals with the Lower Rhine Graben. In this area, we started from EDSF13, already based on a local fault model (Vanneste et al., 2013), and updated the slip rate of several faults based on more recent data (Gold et al., 2017).

Dataset #11: This dataset covers the northwestern African region (Morocco, Algeria, and Tunisia). In this region, we mainly relied on EDSF13 with updates of a few faults in the Moroccan region based on the GEM Global Active Faults Database (Styron and Pagani, 2020) and various other works (Gomez et al., 1996; Akoglu et al., 2006; Rigby, 2008; van der Woerd et al., 2014; Pastor et al., 2015) for refining several fault parameters.

Dataset #12: The NOAFAULTS database (Ganas, 2022) was used to integrate the dataset in the Aegean region for faults not already included in GreDaSS. This dataset was built gradually since 2013 (Ganas et al., 2013) following a fault-trace (polyline) approach with significant upgrades whenever compiled fault maps were available, including faults activated during seismic sequences in the Aegean (Ganas et al., 2018).

Dataset #13: This dataset covering Portugal and offshore regions was updated based on recent works in the Lower Tagus Valley Fault Zone (LTVFZ) (Canora et al., 2015) and Algarve (Sanz de Galdeano et al., 2020).

Dataset #14: This dataset covers most of the Iberian region, including the Pyrenees. In this region, we relied on the Quaternary Faults Database of Iberia (QAFI) database (García-Mayordomo et al., 2012, 2017; IGME, 2015). Due to the different strategies of fault mapping used in QAFI, we redrew the fault traces by interpolation.

Dataset #15: This dataset deals with Slovenia and its surroundings. In this area, we relied on the recently published Database of Active Faults in Slovenia (Atanackov et al., 2021) and the seismogenic fault source model (Atanackov et al., 2022) prepared for the 2021 seismic hazard model for Slovenia (Šket Motnikar et al., 2022). This dataset provides the seismic component of the slip rates.

Dataset #16: This dataset covers Anatolia and parts of the Middle East. In this region, we relied on recent data from the project EMME and data from the national update of the Turkish hazard model (Danciu et al., 2018; Demircioğlu et al., 2018; Emre et al., 2018).

## 2.2 Procedures for crustal faults

The location and geometry of the mapped feature must be available through a set of coordinate pairs in a recognizable geographic coordinate system. The depth extent of the fault plane must have also been provided or derivable. The strike or dip direction, or any alternative strategy to provide data complying with the right-hand rule (e.g., ordered sequence of nodes forming the mapped feature), and the dip angle were also indispensable to complete the geometric reconstruction of the fault plane in three dimensions. Regarding the fault behavior, the required parameters were the rake angle (or at least the prevailing sense of movement) and the slip rate.

The strategy outlined above also adopted a set of prioritization criteria. The highest priority for collating the different datasets was given to the pan-European dataset because it guaranteed maximum spatial coverage with minimum effort. Then, in replacing or extending this initial dataset, we incorporated new data with progressively lower priority given to data that were publicly available within the timeframe of the project, followed by voluntarily contributed datasets from the community, and lastly by solicited local contributions where necessary. In handling the possible multiple contributions over the same areas, we prioritized newer data, national data when the dataset covered a specific country, level of accuracy and justification for the requirements listed above, and coherence with surrounding datasets.

Thus, these criteria were applied to collate and harmonize the datasets, fill gaps, resolve overlaps, and remove inconsistencies. Once the collated dataset was obtained, the performed data processing aimed to extract relevant information from the different datasets and convert it into the EFSM20 format, identify the possible duplicates, and assign the ID to each retained record.

The mapped features were resampled to obtain an evenly-spaced single-trace polyline with an average distance between consecutive nodes of ~5 km (Figure 2). Based on common fault scaling relationships (Wells and Coppersmith, 1994; Leonard, 2010, 2014; Allen and Hayes, 2017; Thingbaijam et al., 2017), this length enables us to capture with sufficient accuracy the smallest earthquake ruptures commonly modeled in most hazard analyses using fault sources. The even spacing also ensures that the fault-source total length is measured consistently, regardless of the subjective mapping strategy adopted in the original datasets. The fault trace nodes were sorted based on the average strike (or dip direction) to comply with the right-hand rule (Aki and Richards, 1980). The strike values were then recalculated to reflect the variability of the re-mapped fault.

210
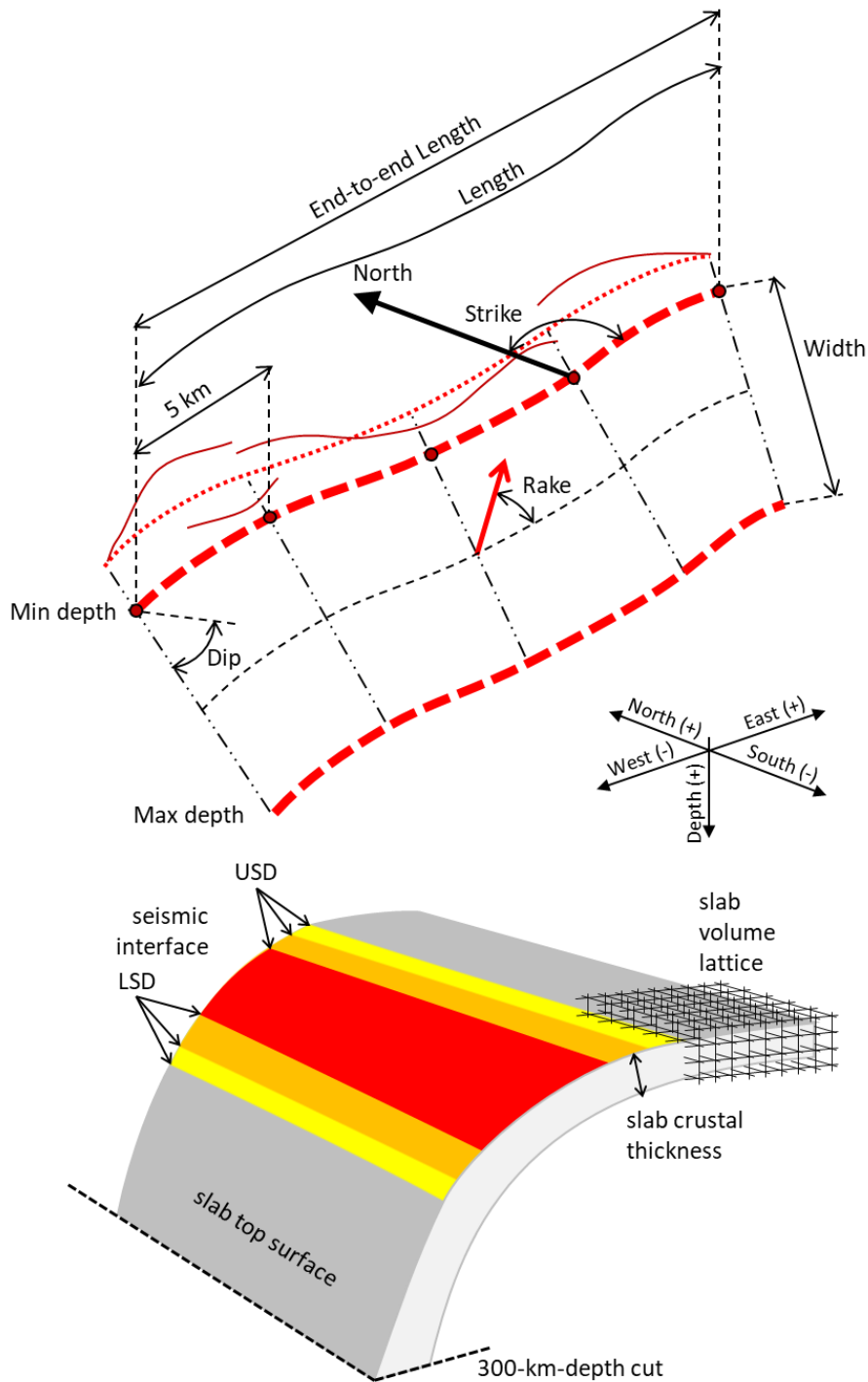
**Figure 2: Cartoon showing the main geometric elements of crustal faults (top) and subduction systems (bottom). See the main text for a complete list of parameters and their descriptions.**

With this revised geometry, we determined the complexity index *c*, which is calculated as

$$c = (1 - L'/L) \cos \delta \qquad (1)$$

where $L'$ is the end-to-end fault length, $L$ is the fault trace length, and $\delta$ is the reported dip angle (Figure 2). This complexity index tends to be close to zero when the fault tends to be nearly straight or vertical. It can contribute to better evaluating whether to adopt the simple- or complex-fault models when using the OpenQuake software (Pagani et al., 2014) for modeling seismic hazards. The crustal fault complexity index returned 174 faults with a value equal to zero. This value is due to a dip equal to 90 degrees for 62 cases and a rectilinear trace for the remaining 112. Only 6 faults have a complexity index larger than 0.1.

We verified the depth datum (local ground surface or mean geoid/spheroid), then checked the possible intersections of the reported upper depth with the topo-bathymetry using the ETOPO1 Global Relief Model (Amante, 2009; NOAA National Geophysical Data Center, 2009), and the reported lower depth with the base of the crust using the European Moho (Grad et al., 2009). We also searched for possible down-dip intersections of different fault planes (e.g., two faults cross-cutting each other at depth). Occasionally, when the faults determined an unrealistic structural configuration, we removed or modified parts of the interested faults.

A one-letter or two-letter code indicates the fault sense of movement: N for normal (-135° ≤ rake ≤ -45°), R for reverse faulting (45° ≤ rake ≤ 135°), RL for right-lateral transcurrent (135° < rake < -135°), LL for left-lateral transcurrent (45° > rake > -45°). These four classes were also reduced to two classes, using the two-letter code DS for dip-slip faulting (normal and reverse) and SS for strike-slip faulting (right- and left-lateral) to ease the application of the fault scaling relations.

The tectonic characterization of crustal faults includes defining three types of tectonic settings: interplate region, stable continental region, and Mid-Atlantic Ridge, identified by the three-letter codes: INT, SCR, and MAR, respectively. For the geographic distribution of the SCR, we started from the mapping made by (Johnston, 1994) and refined the INT and MAR based on the plate tectonic model by (Kagan et al., 2010) and local geology where needed.

Since some of the original datasets only reported a single value of the dip angle for several faults, we extrapolated the dip angle variability from all the other records in the fault collection. We thus calculated the dip angle variation ratio of reported values and then applied it to extrapolate the dip uncertainty range around single-value dip angles, assuming the reported single value as the average dip. The dip variation ratio ($R\delta$) for each fault is calculated as

$$R\delta = \frac{\delta_{max} - \delta_{min}}{2} / \delta_{avg} \qquad (2)$$

where $\delta$ is the dip angle value of all faults with $\delta_{max} - \delta_{min} > 0$. We did this calculation separately for dip-slip and strike-slip faults. The dip harmonization procedure used 660 dip-slip faults to determine an average dip variation ratio of 0.21 and 236 strike-slip faults to determine an average dip variation ratio of 0.12. These two values were then applied to incorporate the range of dip variability in the remaining 195 dip-slip faults and 157 strike-slip faults.

Once the minimum and maximum depths and dip angles are determined, the fault width can be calculated using simple trigonometry.

Also, in the case of the slip rate, several records of the original datasets only reported a single value, and thus we adopted the same approach. The slip-rate variation ratio ($R\dot{D}$) for each fault is calculated as

$$R\dot{D} = \frac{\dot{D}_{max} - \dot{D}_{min}}{2} / \dot{D}_{avg} \tag{3}$$

where $\dot{D}$ is the slip rate value of all faults with $\dot{D}_{max} - \dot{D}_{min} > 0$ and $\dot{D}_{min} > 1E - 4$ mm/yr (the latter assumed as a lower threshold for considering the fault activity. We did this calculation separately for the four different combinations of slip type (DS and SS) and tectonic setting (INT and SCR). Then we calculated the weighted average based on the number of faults in the four groups. The slip-rate harmonization procedure used 970 faults out of the 1109 INT and SCR faults to determine a weighted average slip-rate variation ratio of 0.51 that was then applied to the remaining 139 faults, including the Gloria Fault (Dataset #02). The 138 MAR faults were excluded from the slip-rate harmonization because of their peculiar tectonic setting, which, differently from the rest of crustal faults, involves exclusively oceanic crust. The weighted average slip-rate variation ratio for these faults is 0.46.

The maximum earthquake magnitude of a crustal fault is estimated as the magnitude value, in the moment magnitude scale, that corresponds to the largest possible rupture that the fault can host based on its dimensions and the magnitude scaling relations by (Leonard, 2010, 2014), which also incorporate the rupture aspect ratio. In the adopted scaling relations, the moment magnitude ($M_w$) is determined by an equation in the form of

$$M_w = a + b \log(S) \tag{4}$$

where $S$ is the size of any of the following rupture dimensions: end-to-end length, width, area, or displacement, and the parameters "$a$" and "$b$" take different values depending on the $S$ type, the sense of slip (DS and SS), the seismotectonic context (INT or MAR, and SCR). Estimating the maximum earthquake magnitude of fault sources takes three steps. In the first step, we retrieve the fault width ($W$) and preliminarily assume that this value can be the maximum rupture width. Bringing in the rupture aspect ratio, we obtain the rupture length ($L$) required by a rupture of the retrieved width using the scaling relations (Leonard, 2010, 2014). Then we calculate the maximum rupture area ($A$) based on the obtained length and width. These calculations are repeated for the minimum, average, and maximum fault dimensions and retain three magnitude values corresponding to the scaling expected value, plus and minus one standard deviation. In the second step, we calculate the distribution of magnitude deviations ($\Delta M_w^- = avgM_w - minM_w$) and ($\Delta M_w^+ = maxM_w - avgM_w$) from the average for all faults. A preliminary inspection of these deviations showed that the $\Delta Mw$ distributions were strongly skewed, therefore we considered values above the 95th percentile (corresponding to $\Delta Mw > |0.5|$) to be outliers and removed them. In the third step, we obtained the updated distributions of percentile ranks and extracted the 2nd and 5th percentiles of the negative deviations and the 95th and 98th percentiles of the positive deviations and apply them to the average magnitude already calculated.

Finally, the seismic moment rate ($\dot{M}_s$) can be calculated based on the following classic formulation:

$$\dot{M}_s = \chi \dot{M}_g = \chi \mu L W \dot{D} \qquad (5)$$

where $\chi$ is the seismic efficiency, or seismic coupling (Kagan and Jackson, 2013), $\dot{M}_g$ is the geologic moment rate, $\mu$ is the rigidity, $L$ and $W$ are the fault length and width, respectively, and $\dot{D}$ is the long-term slip rate. The applied rigidity is the global crustal average of 33 GPa (Dziewonski and Anderson, 1981), which is also the rigidity used for deriving the magnitude scaling relations (Leonard, 2010, 2014). We use the term seismic efficiency to indicate a coefficient between 0 and 1 that quantifies how much of the total moment rate is to be converted into a seismic moment rate and ultimately into an earthquake rate forecast. This coefficient is often called seismic coupling, but we avoid using it because it also has various meanings (Wang and Dixon, 2004). The information on slip rate values was adopted in bulk from large datasets of regional compilations, and it is therefore obtained using very heterogeneous estimation approaches. In some data sets, slip rate values correspond to the total (seismic and aseismic) slip, whereas fault slip rates of other data sets correspond to only their seismic part. Therefore, the seismic efficiency was not assigned to individual faults in this dataset. This implicitly means that for the moment rate calculations, the seismic efficiency is as if it was equal to 1, and it is thus left to the users to choose a value to apply in their applications.

## 2.3 Subduction-system datasets

Dataset #01: This is the original database EDSF13, compiled in the framework of the SHARE project (Basili et al., 2013), which covered the subduction systems in the eastern Mediterranean region. This dataset was adopted as the starting point to build the new subduction system models for the Hellenic and Cyprus Arcs. The geometry of both slabs were recently revisited in the framework of a tsunami hazard project (Basili et al., 2021). These datasets have also been re-examined in light of the SLAB 2 model (Hayes et al., 2018) and several other slab geometry reconstructions (Ganas and Parsons, 2009; Halpaap et al., 2018, 2019; Sachpazi et al., 2016).

Dataset #02: This dataset corresponds to the most recent version of the DISS (DISS Working Group, 2021), which includes an updated reconstruction of the Calabrian Arc slab geometry based on a rich dataset of seismic reflection profiles for the shallower part (<20 km depth) and the seismicity distribution for the deeper part (Maesano et al., 2017).

Dataset #03: This dataset is an original elaboration of the Gibraltar Arc based on published works. The geometry of the slab was reconstructed using different datasets at different depths. For the shallowest depths, we used data from bedrock markers based on interpreting multichannel seismic reflection profiles and wide-angle seismic surveys (Gutscher et al., 2009), assuming that the top of the slab coincides with the top of the basement. For the intermediate depths (12-40 km), we used a model of the Moho obtained from a set of diverse datasets using a probabilistic surface reconstruction algorithm (Arroucau et al., 2021) and considering typical values for the old Tethys oceanic crust in the range of 7-9 km (Sallarès et al., 2011). Then, we obtained the slab position between 40-70 km depth by interpolating seismicity clusters from the ISC earthquake catalog (ISC, 2019). Within the 140-200 km depth range, the slab was assumed to be vertical based on a tomographic model (Civiero et al., 2018), which shows a nearly vertical high-velocity p-wave anomaly down to 600 km deep.

## 2.4 Procedures for subduction systems

Subduction systems form at convergent plate boundaries where one plate, the slab, sinks below the other. In these complex
systems, different types of earthquake sources co-exist (Satake and Tanioka, 1999).

In this compilation, we assume that the crustal fault sources deal with the earthquakes occurring in the upper plate of a
subduction system. We thus designed the subduction system model to address both the subduction interface and the intraslab
seismicity (Figure 2). To this end, we first focused on reconstructing the three-dimensional geometry of the lower plate top
surface and its crustal thickness. Then, we added a set of basic parameters required for addressing the tectonic behavior, such
as the upper and lower depths of the seismic interface and the net convergence direction and rate.

This type of reconstruction is typically performed using data from geology, exploration geophysics, seismicity distribution,
and seismic tomography. The mapped feature must be available through a set of coordinate triplets, typically latitude,
longitude, and depth, in a recognizable geographic coordinate system (e.g., scattered points, lattice, isolines, triangular
meshes). The adopted 3D geometries were resampled at regular spacing and smoothed to ensure the same spatial resolution in
the different models. Evenly-spaced isolines were then used to represent the slab top surface. The average distance between
consecutive nodes of each isoline was set at 5 km. The isoline depth interval was set at 1 km above 40 km depth and 10 km
below 40 km. The deepest slab isoline was fixed at 300 km depth. The slab geometry is completed by assessing the crustal
thickness of the lower plate measured in the outermost part of the subduction zone, near the tip of the accretionary wedge, by
taking the base of the crust as a reference from the European Moho (Grad et al., 2009) model for consistency with that used
for the crustal faults. For the sake of simplicity, the crustal thickness so measured is assumed to be constant in the rest of the
subducted slab to derive the lower plate bottom surface. The volume between the lower plate top and bottom surfaces is then
resampled by a lattice of evenly-spaced nodes at a 10 km distance in all directions. The uppermost depth of the lattice was
fixed at 5 km to ensure a consistent sampling of the shallower and gentler part of the slab.

The subduction interface parameterization includes the treatment of uncertainties based on the logic tree schema shown in
Figure 3, including three alternative estimates of each parameter.

To estimate the upper depth of the seismic interface, we considered data about the location of the 100-150°C isotherm, the
position of the contact between the lower plate and the overlaying softer sediments, the position of splay-fault branching, and
the seismicity cutoff depth; whereas to estimate the lower depth of the seismic interface, we considered the location of the
intersection of the lower plate with the Moho of the upper plate, the location of the 350-450°C isotherm, and the seismicity
cutoff (Di Stefano et al., 1999; Gutscher et al., 2006; Thiebot and Gutscher, 2006; Grad et al., 2009; Syracuse et al., 2010;
Heuret et al., 2011; Davies, 2013). When multiple estimates from different data types were available, we assigned a higher
weight to the Moho intersection and a lower weight to thermal and other models. We then obtained a weighted average of the
minimum, intermediate, and maximum values retrieved from various literature sources.

The maximum earthquake magnitude of the seismic interface is estimated as the magnitude value, in the moment magnitude
340    scale, that corresponds to the largest possible rupture that the seismic interface can host based on its area and magnitude scaling
relations (Allen and Hayes, 2017).

The rigidity (shear modulus) depth-dependence from different datasets (Dziewonski and Anderson, 1981; Scala et al., 2020;
Bilek and Lay, 1999; Sallarès and Ranero, 2019) are reported in Figure 4 (left), showing the rigidity variation within the
common depth interval of the subduction interface of the four subduction systems.
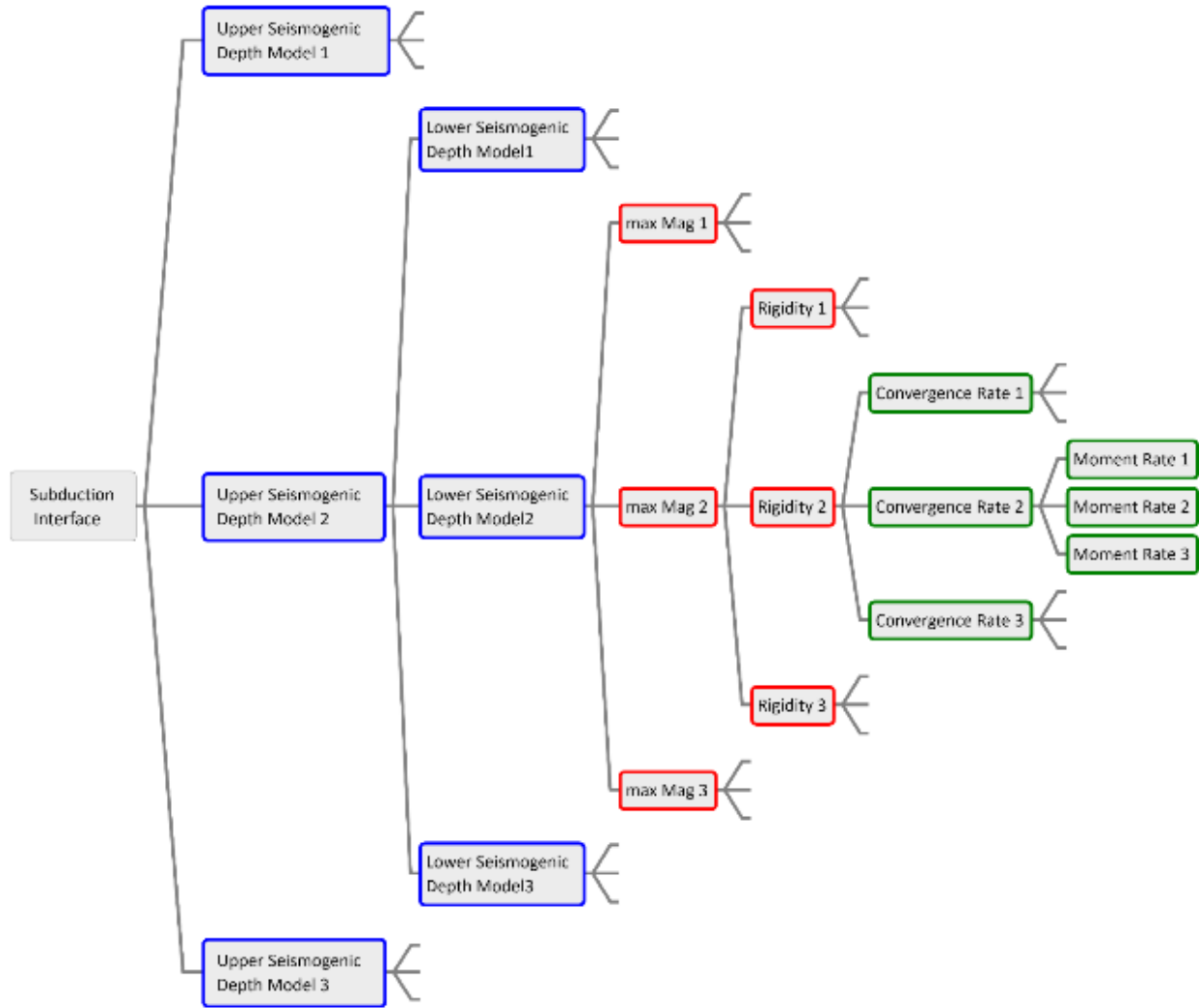
345

**Figure 3: Logic tree to handle the parameter uncertainty in the different realizations of the subduction interfaces. This scheme
implies nine geometric realizations with different areas spanning different depth ranges, implying 27 alternatives of maximum
magnitude and rigidity. Considering the three alternative convergence rates yield 81 moment-rate alternatives. The logic-tree
outcomes provide 243 moment-rate and maximum-magnitude combinations for exploring the earthquake rate forecasts based on**
350    **seismic-moment balanced recurrence models. (Figure prepared with XMind software)**

The convergence direction and rate were estimated by geodetic measurements (velocity vectors) and/or by modeling the relative motion of the upper and lower plates across the subduction interface, as available in the literature (Carafa et al., 2018; Devoti et al., 2008; Hollenstein et al., 2008; Howell et al., 2017; Nocquet, 2012; Palano et al., 2015; Reilinger et al., 2006; Stich et al., 2006; Wdowinski et al., 2006) across the subduction systems (Figure 4 right). The values from different sources were weight-averaged based on the length of the subduction interface sector over which the values were measured or estimated. The goal was to agnostically capture the plate convergence order of magnitude and its possible variability range, rather than finding the best estimates. Assuming that the subduction interface cannot be faster than the plate motion, these values were used as simple indicators without any further processing, neither the modeled convergence was differentiated based on the modeling approach (e.g., block modeling vs. kinematic finite element modeling).
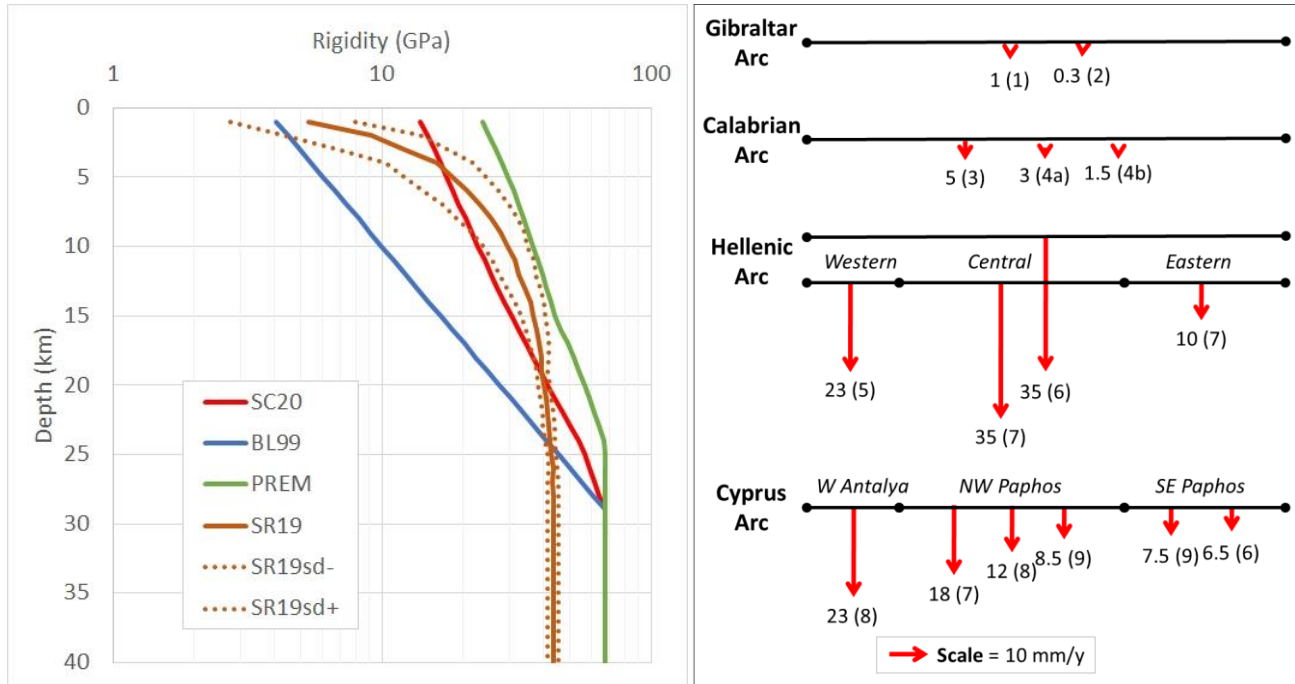
**Figure 4: (left) Depth-dependent rigidity in subduction zones from various authors. SC20, BL99, PREM, SR19. (Dziewonski and Anderson, 1981; Scala et al., 2020; Bilek and Lay, 1999; Sallarès and Ranero, 2019). (right) Synoptic view of the velocity vectors in the four subduction systems. Arrow sizes are scaled according to the reported velocity (all in mm/yr). Number in parentheses represents different works: 1) Stich et al. (2006); 2) Palano et al. (2015); 3) Devoti et al. (2008); 4a,b) Carafa et al. (2018); 5) Hollenstein et al. (2008); 6) Nocquet (2012); 7) Reilinger et al. (2006); 8) Howell et al. (2017); 9) Wdowinsky et al. (2006). In the case of Carafa et al. (2018): a = if creeping, b = if temporarily locked.**

Similarly to crustal faults, the seismic moment rate is estimated using the classic formulation reported in Eq. (5). However, in the subduction case, $\dot{D}$ is the long-term convergence rate, and the rigidity ($m$) varies with depth within the upper and lower depth limits of the subduction interface. The seismic efficiency was not assigned in this dataset; thus, the distributed dataset thus reports the total moment rate. This implicitly means that for the moment rate calculations, the seismic efficiency is as if it was equal to 1, and it is thus left to the users to choose a value to apply in their applications.

# 3 Results

## 3.1 EFSM20 data compilation

The EFSM20 final compilation covers an area spanning from the Mid-Atlantic Ridge to the Caucasus and from northern Africa to Iceland, counting 1,248 crustal faults - for a total length of ~95,100 km. Thanks to the continuous work on active faults in many regions, and the continual update of regional databases, we were able to obtain a much richer fault-source model with respect to EDSF13, which counted 1,128 crustal faults - for a total length of ~63,775 km. Of the cumulative EFSM20 crustal-fault length, 55,401 km are onshore. Of the 39,699 km offshore, 22,846 km are in the Atlantic Ocean and 16,853 km in the Mediterranean Sea, the Black Sea, and the Caspian Sea. EFSM20 also includes four subduction systems, for a total length of the subduction interface of ~2120 km. Three subduction systems in the eastern Mediterranean Sea were already present in the EDSF13 starting dataset, and a new one was added in the Gibraltar Strait. The classification per tectonic setting and slip type is summarized in Table 1.

**Table 1 EFSM20 fault-sources summary.**

|  | DS No. | DS km | SS No. | SS km | All No. | All km |
|---|---|---|---|---|---|---|
| INT | 709 | 45,578 | 341 | 23,565 | 1,050 | 69,143 |
| MAR | 94 | 17,018 | 45 | 5,241 | 139 | 22,259 |
| SCR | 52 | 2,921 | 7 | 778 | 59 | 3,699 |
| Total CF | 855 | 65,516 | 393 | 29,584 | 1,248 | 95,101 |
| Subd. Systems | 4 | 2,120 |  |  | 4 | 2,120 |
| Grand total | 859 | 67,636 |  |  | 1,252 | 97,221 |

Figure 5 shows the crustal faults' geographic distribution and frequency of relevant behavior parameters (faulting type, slip rate, moment rate, and maximum magnitude). Slip rates and moment rate maps provide an overview of the location of the most active faults, generally aligned with the major plate boundaries. Conversely, moving away from the plate boundary toward the plate interiors, one finds progressively less-active faults. The average maximum magnitude distribution (Figure 5, lower-left panel) is somehow left-skewed, indicating that the crustal faults' hosting the largest magnitude potential are very rare. Although most of the highest maximum magnitude values are found on faults aligned with plate boundaries, several large values are also found in the plate interiors. This circumstance occurs because the adopted method reflects the size of the fault and not any other property.

Figure 6 shows the 3D geometric reconstruction of the four slabs. Overall, the seismic interface is confined at depths between 6 and 39 km. The 3D geometry and the upper and lower depths of the seismic interface were the main constraints for determining the size of the largest rupture and its associated moment magnitude based on the scaling relations. The obtained maximum magnitude values vary from a minimum of 7.98 in the Calabrian Arc to a maximum of 9.17 in the Hellenic Arc.
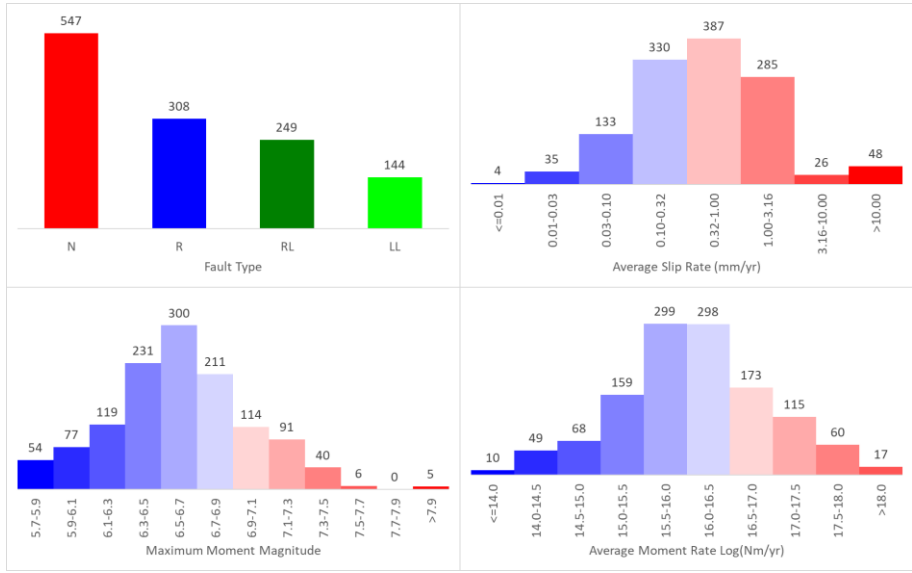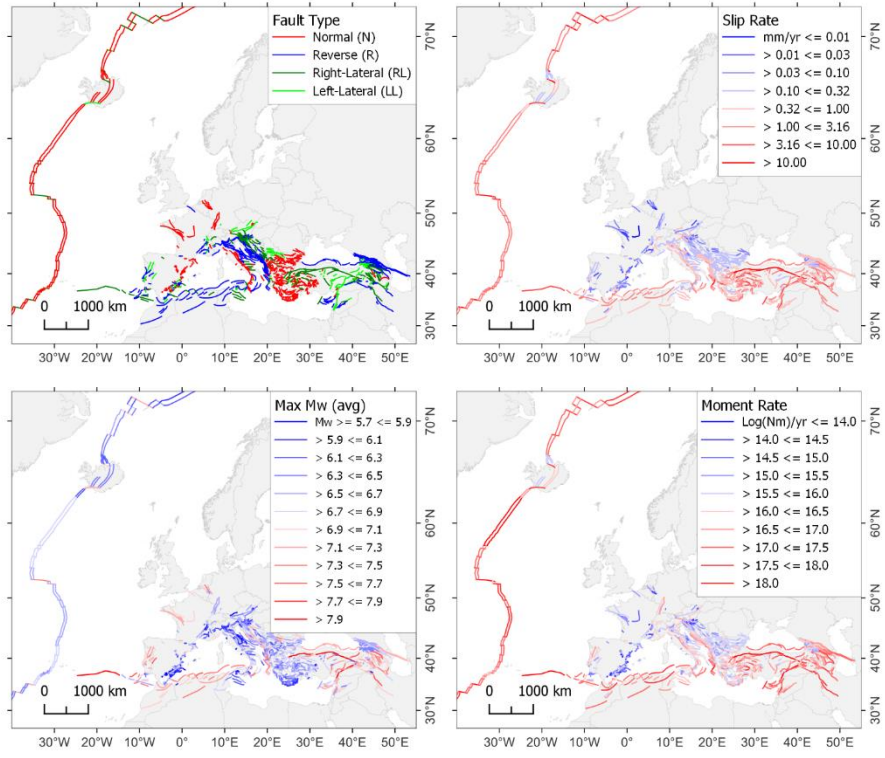
**Figure 5: Maps (upper panels) and histograms (lower panels) of the EFSM20 crustal faults color-coded according to faulting type (upper left), average slip rate (upper right), maximum moment magnitude (lower left), and average moment rate (lower right). Color classes are the same as those distributed by OGC WMS web services. (See Appendix B for a large version of these maps).**

The uncertainties on the area and the scaling relations provide 27 combinations per subduction interface, yielding an overall variability between 0.66-0.86 magnitude units. Regarding convergence rates, we recall that although some reported values concern different sectors of the subduction interface, EFSM20 reports a single value and associated uncertainty for the entire arc. The obtained average values vary from a minimum of ~1 mm/yr in the Gibraltar Arc to a maximum of ~24 mm/yr in the Hellenic Arc. Combining the variability associated with the calculation (rigidity, area, and convergence rate) leads to 81 alternatives for each subduction interface. The resulting moment rates vary from a minimum of 4.5E+17 Nm/yr in the Gibraltar Arc to a maximum of 1.9E+20 Nm/yr in the Hellenic Arc. Each subduction system's largest moment rate value is 3-5 times larger than its smallest value. Figure 7 summarizes the moment rate and maximum magnitudes for crustal faults, grouped in various classes, and subduction interfaces showing the overall variability of these key parameters for the entire dataset.
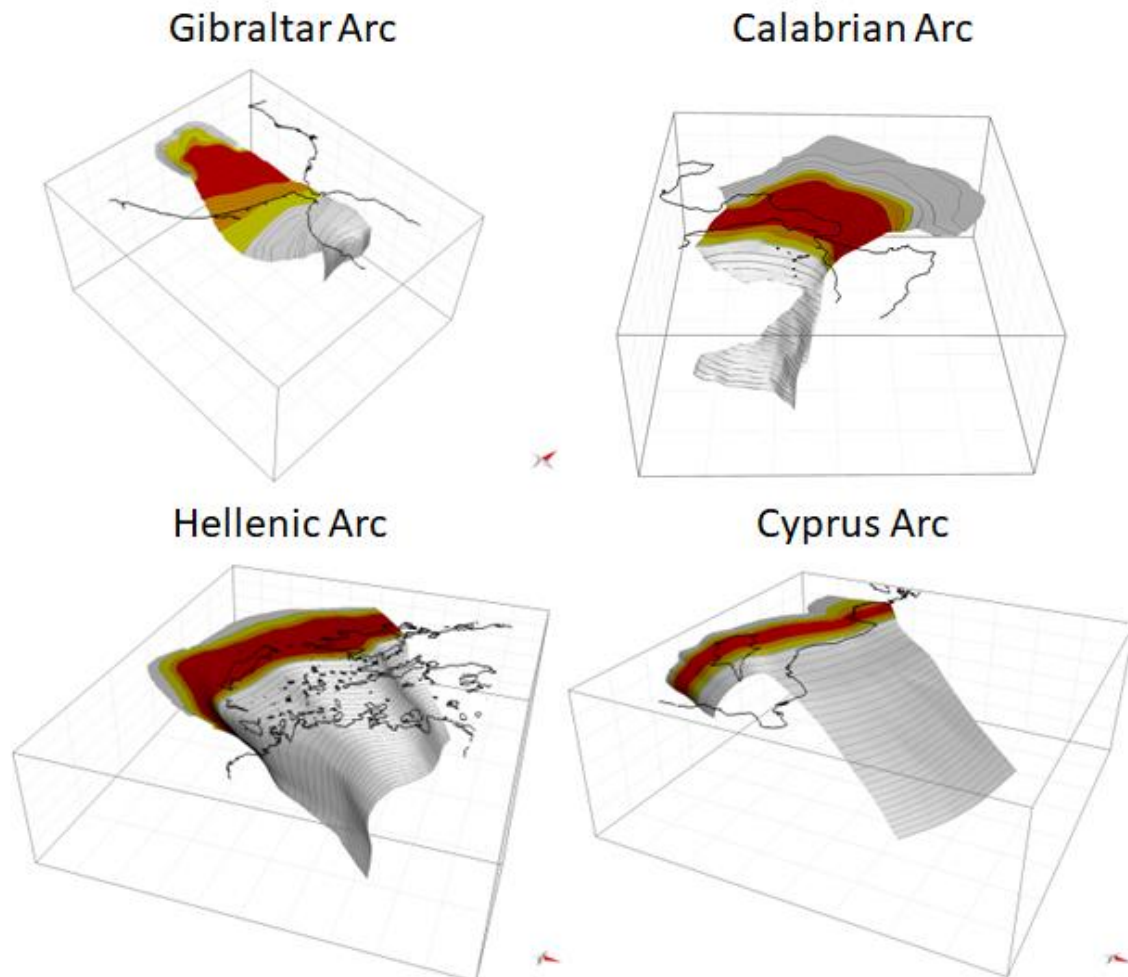
**Figure 6: Oblique views of the tri-dimensional geometry of the four slab models. The vertical extent of all boxes is 300 km. The colored part of the slab top surface represents the extent of the seismic interface, including the uncertainty of the upper and lower seismogenic depths represented by color bands as indicated in Figure 2.**
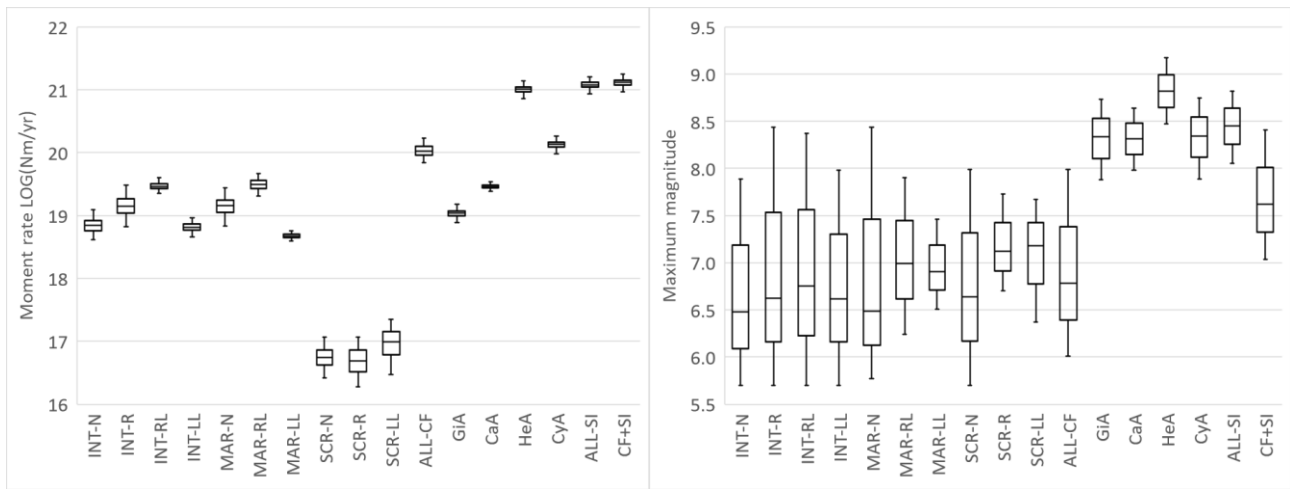
415 **Figure 7: Box-and-whisker charts of the moment rate (left-hand panel) and maximum magnitudes (right-hand panel) for crustal faults, grouped in various classes, and subduction interfaces. Boxes indicate the variability between the median and the upper and lower quartiles; whiskers indicate the variability outside the quartiles. Legend: INT = interplate; MAR = Mid-Atlantic Ridge; SCR= stable continental region; N = normal, R = reverse; RL = right lateral; LL = left lateral; CF = crustal faults; GiA = Gibraltar Arc; CaA = Calabrian Arc; HeA = Hellenic Arc; CyA = Cyprus Arc (CyA); SI = subduction interfaces.**

### 3.3 EFSM20 data-products sharing portfolio

420

The outcomes of collation, harmonization, and derived-parameter characterization of all fault sources form a portfolio of datasets publicly shared for download (GeoJSON files, ESRI shapefiles, MapInfo tables) and via web services (WFS and WMS) adopting the OGC standards (Table A1 and Table A2).

Crustal fault sources also include the geometric extrusion of the fault plane within the minimum and maximum depths in the

425 direction normal to the fault trace. Key elements of the fault plane are the vertical projection onto the ground surface of the top and bottom traces, the midline trace, the polygon enclosing the fault plane, and depth isolines. These geometric features are provided in different files, including all the key parameters illustrated in the previous section as tabulated attributes. The depth isolines have a 0.5 km spacing interval and include the nominal depth as an attribute.

The subduction systems include the geometric representation of the slab top surface by depth isolines and the slab by a cubic

430 lattice. The depth isolines are at 1 km spacing between 0-40 km depth and 10 km spacing between 40-300 km depth. The side of the cubic lattice is 10 km, and each lattice node also provides the slab strike, dip-direction, and dip. The subduction systems, in addition to the geometry of the top surface of the slabs, include datasets for the subduction interface parameters, the discretization, and the various realizations considered using the logic tree shown in Figure 3.

Table A1 summarizes the content of these datasets, including a link to the attribute definitions of each file (Tables A3, A4,

435 A5, A6, A7, A8, A9).

Table A2 summarizes the data made available only via OGC WMS. These are styled map layers ready-to-use to display color-coded relevant parameters of the fault sources. The adopted styles are provided to the users in the Styled Layer Descriptor (SLD) format. These style files can be re-applied to the downloaded files or to the WFS layers to recreate the styled maps.

The main access point to this dataset is the European Databases of Seismogenic Faults portal (https://seismofaults.eu/efsm20).
Other access points for the dataset are the EFEHR portal (http://www.efehr.org/start/) and the EPOS ICS-C data portal (Bailo et al., 2023) (https://www.ics-c.epos-eu.org/).

## 4 Discussion

### 4.1 Lessons learned from the compilation and harmonization

The compilation of EFSM20 represents a substantial update and advancement of EDSF13. EFSM20 improved along the boundary around the European plate and within the plate interiors, focusing on the region within a 300-km-wide buffer around European countries. Within this buffer, the compilation was simplified in Iceland and certainly lacking in the Azores, mainly due to the complex volcano-tectonic processes and limited knowledge of active structures. Also lacking is the region of the Hellenic Arc and Cyprus Arc accretionary wedge, where seismic sources, such as splay thrust faults and back-thrusts, are known to exist, but their systematic mapping would require a dedicated effort due to the large extent of the region, its offshore location, and complex deformation that characterize accretionary wedges in general, and a very broad and fast-growing one in this case (>300 km at 10 mm/yr) due to the long duration (>35 Myr) of the subduction process (Kastens, 1991).

Concerning crustal faults, we identified several regional datasets that vary in date of the latest release, geographical extent, level of fault characterization, and data formats. In addition to those listed in the final compilation, several other datasets were considered, such as, for example, those covering Romania and the northern Black Sea (Diaconescu et al., 2019a, b, 2021), Iceland (Bayat et al., 2022) or the Caucasus (Onur et al., 2019, 2020). Although these datasets represented a significant advancement relative to EDSF13, they could not be used because we could not work out the compliance with the requirements above recalled within the project timeframe.

The fault information in certain areas has already improved due to recent work not included in this release, such as, for example, the northern Adriatic region (Panara et al., 2021), which included a better-constrained version of the fault that ruptured in the Mw 5.5 earthquake (Maesano et al., 2023) on 9 November 2022 in the Northern Adriatic Sea. The depth extent of the Hellenic Arc subduction interface and its relation with the maximum depth of the crustal faults in the Aegean region could be improved using rheological models (Maggini and Caputo, 2020, 2021). Likewise, newer geodetic data are now available to help refine the convergence rate across the Hellenic Arc (Briole et al., 2021). Other improvements or corrections can also be expected from post-earthquake surveys and analyses of significant recent seismic events such as, among others, the Petrinja (Croatia) Mw 6.4 earthquake on 29 December 2020, the Marrakesh–Safi (Morocco) Mw 6.8 earthquake on 8 September 2023, or the Mw 7.8 earthquake the on 6 February 2023 struck the Turkey-Syria border region. Also, some known errors are present, such as the case of the Averroes fault in the Alboran Sea (IDFS: ESCF03E; IDDS: #4). This fault was introduced as reported in an earlier version of QAFI and escaped a recent update that, although confirming the fault trace, revised the dip, dip direction, and kinematics (Perea et al., 2018). These and possibly other cases should be taken into consideration for future updates.

470 The total moment rate in EFSM20 of crustal faults and subduction interfaces combined is in the order of 1.3E+21 Nm/yr (Figure 7). The crustal faults take up to about 8%, and the subduction interfaces 92% of this amount. Among the former, the moment rate attributable to the SCR is 0.2%, and the rest is almost equally partitioned between the MAR and the rest of the INT. Among the latter, instead, more than 85% of the total subduction interface moment rate is taken up by the Hellenic Arc. The contribution of intraslab tectonics is excluded from the total moment rate because intraslab faults were neither individually

475 mapped nor was their slip rate determined.

We recall that slip rate is the amount of slip as a function of geologic time; in other words, slip rate is obtained by dividing the amount of fault displacement, as determined from geodetic measurements, from offset man-made structures, or from offset geologic features, by time interval during which that offset has taken place (Morell et al., 2020). Generally, reported slip rates from geologic studies include the cumulative slip of individual seismic events and any aseismic slip on the fault (e.g., pre-

480 and/or post-seismic slip and aseismic slip at the surface). These components are hardly distinguishable in the geologic record. In common practice encountered in the collected datasets, slip rate data come from a limited number of point observations that are accepted as representing some presumed average displacement along strike. Studies that report accurate slip rate variations along strike are relatively rare, and those that report the slip variations with depth or along dip are even much rarer (Finocchio et al., 2016). Therefore, moment rate estimates in EFSM20 generally refer to the tectonic component, and the actual seismic

485 moment rate to be converted in an earthquake rate forecast could be somewhat smaller depending on the seismic efficiency in Eq. 5. This parameter is not explored here. Users are thus cautioned about the possibility that some crustal fault slip rates, as in the case of Dataset #15 or others derived from the literature, could have already been "cleaned" by a predetermined or modeled seismic efficiency. This occurrence may not have been evident when the information on slip rate values was adopted in bulk from a large dataset of a regional compilation. In this respect, it is worth recalling that seismic efficiency can

490 dramatically influence earthquake productivity, especially for the subduction interfaces. For example, the seismic efficiency of the Hellenic Arc is generally considered weak (Shaw and Jackson, 2010; Heuret et al., 2011; Reilinger et al., 2010; Becker and Meier, 2010; Rontogianni, 2010), as moment rate based on seismicity accounts only for about 20% of the moment rate based on the convergence rate shown by geodetic data. However, complete seismic coupling was proposed for the northwestern termination of the subduction beneath the Ionian Islands (Laigle et al., 2002; Ganas et al., 2020; Briole et al., 2021), suggesting

495 possible lateral variations of seismic coupling along the Hellenic Arc (Laigle et al., 2004), in contrast with proposals of full coupling characterizing the entire Hellenic Arc (Ganas and Parsons, 2009). The seismic efficiency of the Calabrian Arc is also very variable. Based on geodetic observations and geodynamic modeling, the Calabrian Arc was hypothesized to be either locked or partly locked (Carafa et al., 2018) or negligibly active (Nijholt et al., 2018). Also, different interpretations exist on the activity of the Gibraltar Arc subduction interface. For example, the QAFI dataset does not include the Gibraltar subduction

500 system, and other studies on geodetic observations do not consider the subduction process active (Stich et al., 2006) or consider it at all (Palano et al., 2015). The convergence rates reported in EFSM20 are thus meant to provide reasonable values in the hypothesis that the subduction interface is active, although EFSM20 remains neutral in this respect. The slab geometric

reconstruction can still be useful for separating crustal seismicity from intraslab seismicity either for geodynamic studies (Goes et al., 2017) or other hazard applications (Basili et al., 2021), since the intraslab tectonic rates were not estimated.

505    The rigidity treatment is the main difference between crustal faults and subduction interfaces in estimating the moment rate. For crustal faults, we considered a uniform rigidity of 33 GPa, according to global estimates and consistency with fault scaling relations (Dziewonski and Anderson, 1981; Leonard, 2010), whereas for the subduction interfaces, we used the depth-dependent rigidity variation as observed in subduction zones from around the world (Bilek and Lay, 1999; Sallarès and Ranero, 2019) and already used to model earthquake ruptures for tsunami simulations and hazards (Geist and Bilek, 2001; Scala et al.,

510    2020). We know that using a uniform rigidity value for crustal faults is not appropriate in certain cases. For instance, evidence shows that the basement offshore SW Iberia is mainly made of exhumed mantle rocks (Sallarès et al., 2013; Martínez-Loriente et al., 2014). However, we decided to use a homogeneous rigidity value due to the large volume of data and the need to homogenize its treatment. Noteworthily, depth-dependent rigidity in EFSM20 subduction systems implies a variation of up to $\pm30\%$ on the moment rate estimates compared to the uniform rigidity approach.

515    The subduction interfaces have systematically higher maximum magnitude than crustal faults (Figure 7), reflecting the larger area of subduction interfaces, which can host larger ruptures. The maximum magnitude informs us of the size of the largest possible rupture that each fault-source can individually host (i.e., excluding the possible interactions among multiple faults) but tells nothing about the likelihood of that magnitude earthquake being released. To that end, a recurrence model should be developed based on the provided characteristics. Notice that the scaling relations of interface earthquakes predict rupture areas

520    about 1.7 times larger, and their average slip is about 0.5 times smaller than those of crustal earthquakes with the same seismic moment. This consideration applies to most scaling relations, not just those used here (Skarlatoudis et al., 2016), and has implications on how the moment rate is partitioned into earthquakes of different sizes and, ultimately, in their recurrence. This reasoning particularly affects the crustal faults in the SCR, where the very low moment rate implies that the occurrence of the largest earthquakes is extremely unlikely and possibly their recurrence of little to nil practical impact on seismic hazard

525    estimates at standard average return periods (475 years).

## 4.2 Outlook

EFSM20 was designed to fulfill the specific needs of a hazard application at the scale of a continent and has thus been one of the main input datasets used for the 2020 update of the European Seismic Hazard Model (ESHM20) (Danciu et al., 2021, 2022). Its predecessor EDSF13 (Basili et al., 2013) was used for the 2013 European Seismic Hazard Model (ESHM13)

530    (Woessner et al., 2015), the first regional tsunami hazard model NEAMTHM18 (Basili et al., 2021), and several other hazard analyses at different scales, post-earthquake analyses, and tectonic modeling. Likewise, EFSM20 is aimed to serve the same scope. To this end, it is distributed as machine-readable files using open standards (OGC), which allow users to port the datasets on various platforms and use them programmatically.

Being a continent-scale compilation, however, EFSM20 implied data selections and simplifications, which may hinder its

535    application at a more local scale. We thus recommend that the users resort to the original datasets and pertinent literature when

performing analysis at a local scale, such as site-specific hazard applications or near-field seismic scenarios. In these regards, one first-order aspect is fault geometry. The down-dip planar simplification is known to generate bias when reconstructing the earthquake ruptures (Dutta et al., 2021) or to underestimate the near-field ground motion (Passone and Mai, 2017). Similarly, tsunami modeling requires full knowledge of the 3D geometry of faults (Gómez de la Peña et al., 2022; Serra et al., 2021; Tonini et al., 2020).

540

The compilation of EFSM20 relied on the efforts made by many scientists in collecting and systematizing data about active faults with a region-wide perspective. Scientists collect most data on potential fault sources country-by-country for practical and organizational reasons. This practice may hardly change, but multilateral collaborations at the country bounders may decrease the need for ex-post data harmonization. The regional element is key for earthquake hazard analyses which need fault-source characterization also in remote or less tectonically active areas. From inspecting the literature, we realized that most works concentrate on the most-active, most-evident geological structures. A more balanced approach seems instead necessary to complement our in-depth knowledge of the most obvious structures along major plate boundaries with a better understanding of the least obvious ones. For example, the plate interiors account for less than 4% of all global seismicity (Kagan et al., 2010), and this estimate from fault sources in EFSM20 is much lower, suggesting that we might still be missing important intraplate faults or misjudging their activity rate or recurrence (Calais et al., 2016). Mitigating earthquake risk in such areas is thus extremely challenging and important (England and Jackson, 2011).

545

550

Active fault identification and characterization are challenging in many respects. In continental interiors, climatic processes, and human activities can easily obliterate the most recent active faulting due to the long earthquake recurrence intervals (Grützner et al., 2017). In moderately active regions along plate boundaries, sedimentation rates can overtake tectonic rates and conceal the fault activity under a thick sedimentary cover (Panara et al., 2021).

555

Nonetheless, even very active plate boundaries are not easily accessible for in-depth analyses. Although EFSM20 includes a large proportion of offshore faults, there is no doubt that offshore fault-source identification and characterization have a large room for improvement (Perea et al., 2021), not only to improve the use of fault sources in tsunami hazard analyses but also to improve the modeling of tectonic systems and the tectonic deformation partition at the transition between onshore and offshore structural systems.

560

**Data availability**

The data presented in this study are available online under the open-access Creative Commons Attribution 4.0 International (CC BY 4.0) license (https://doi.org/10.13127/efsm20, Basili et al., 2022).

## Author contributions

RB drafted the manuscript and most of the figures. All authors read, discussed, and revised the text and figures. CB, DG, KS, LD, RB, SV established the data requirements and designed the data model. Coordinated the datasets acquisition, and harmonization. HJ, MEC, SB contributed original data and insights on crustal faults in France and surrounding regions. NT, SA contributed original data and insights on crustal faults in Georgia and surrounding regions. AG, RC, VT contributed original data and insights on crustal faults in Greece and surrounding regions. BSM, JA, PJR, PZ contributed original data and insights on crustal faults in Slovenia and surrounding regions. VK contributed original data and insights on crustal faults in Slovenia and surrounding regions. Revised data on crustal faults from EDSF in various regions. CC, JGM, RMB contributed original data and insights on crustal faults in Spain and surrounding regions. EG, HP, LG, SML contributed original data and insights on crustal faults in the Gulf of Cadiz and/or the Alboran Sea. MDT contributed original data and insights on crustal faults in Turkey and surrounding regions. JCD contributed original data and insights on crustal faults in the Gulf of Cadiz and/or the Alboran Sea. MN, PA, SC contributed to defining the Gibraltar Arc. MMCC contributed to the characterization of the subduction systems. MMT designed the crustal fault model for the Mid-Atlantic Ridge and Iceland. Revised data of crustal faults in Northern Africa, Greece, and the Ionian Sea. Designed and characterized the subduction systems. KV revised data and contributed insights on crustal faults in the Rhine Graben. FEM revised data of crustal faults in the Ionian Sea. Designed and characterized the subduction systems. RV designed and organized the data distribution through web services, designed the data portal, and validated the consistency of the data distribution with the EPOS requirements. Organized the metadata.

## Competing interests

The authors declare that they have no conflict of interest.

## Acknowledgments

This work started within the project Seismology and Earthquake Engineering Research Infrastructure Alliance for Europe (SERA) which received funding from the European Union's Horizon 2020 Research and Innovation Programme under grant agreement No.730900. Additional resources to this work were received from the Joint Research Unit, EPOS-ITALIA (https://www.epos-italia.it/) Executive Program 2021-2024, funded by the Italian Ministry of University and Research, and from the Multi-Year Collaboration Agreement on Data and Services Provision 2022-2023 between EPOS ERIC and EPOS TCS Seismology and the associated Work Program for 2022 "MYCA22/23DSP-WP22" of the European Facilities for Earthquake Hazard and Risk (EFEHR). We thank the staff and colleagues who manage the EPOS ICS-C for their help in incorporating our data into the EPOS portal. The authors are grateful to the handling editors, Pierre-Yves Bard and Veronica Pazzi, and the reviewers, João Fonseca and Chris Rollins, for their excellent and constructive comments and helpful feedback that significantly improved the quality of the paper.

# References

Aki, K. and Richards, P. G.: Quantitative seismology: Theory and methods., W. H. Freeman & Co, San Francisco, 557 pp., 1980.

Akoglu, A. M., Cakir, Z., Meghraoui, M., Belabbes, S., El Alami, S. O., Ergintav, S., and Akyüz, H. S.: The 1994–2004 Al Hoceima (Morocco) earthquake sequence: Conjugate fault ruptures deduced from InSAR, Earth and Planetary Science Letters, 252, 467–480, https://doi.org/10.1016/j.epsl.2006.10.010, 2006.

Allen, T. I. and Hayes, G. P.: Alternative Rupture-Scaling Relationships for Subduction Interface and Other Offshore Environments, Bulletin of the Seismological Society of America, 107, 1240–1253, https://doi.org/10.1785/0120160255, 2017.

Amante, C.: ETOPO1 1 Arc-Minute Global Relief Model: Procedures, Data Sources and Analysis, https://doi.org/10.7289/V5C8276M, 2009.

Árnadóttir, T., Geirsson, H., and Jiang, W.: Crustal deformation in Iceland: Plate spreading and earthquake deformation, Jökull, 58, 59–74, 2008.

Arroucau, P., Custódio, S., Civiero, C., Silveira, G., Dias, N., Díaz, J., Villaseñor, A., and Bodin, T.: PRISM3D: a 3-D reference seismic model for Iberia and adjacent areas, Geophysical Journal International, 225, 789–810, https://doi.org/10.1093/gji/ggab005, 2021.

Atanackov, J., Jamšek Rupnik, P., Jež, J., Celarc, B., Novak, M., Milanič, B., Markelj, A., Bavec, M., and Kastelic, V.: Database of Active Faults in Slovenia: Compiling a New Active Fault Database at the Junction Between the Alps, the Dinarides and the Pannonian Basin Tectonic Domains, Front. Earth Sci., 9, 604388, https://doi.org/10.3389/feart.2021.604388, 2021.

Atanackov, J., Jamšek Rupnik, P., Zupančič, P., Šket Motnikar, B., Živčić, M., Čarman, M., Milanič, B., Kastelic, V., Rajh, G., and Gosar, A.: Seismogenic fault and area sources for probabilistic seismic hazard model in Slovenia, https://doi.org/10.1594/PANGAEA.940100, 2022.

Bailo, D., Paciello, R., Michalek, J., Cocco, M., Freda, C., Jeffery, K., and Atakan, K.: The EPOS multi-disciplinary Data Portal for integrated access to solid Earth science datasets, Sci Data, 10, 784, https://doi.org/10.1038/s41597-023-02697-9, 2023.

Basili, R., Valensise, G., Vannoli, P., Burrato, P., Fracassi, U., Mariano, S., Tiberti, M. M., and Boschi, E.: The Database of Individual Seismogenic Sources (DISS), version 3: Summarizing 20 years of research on Italy's earthquake geology, Tectonophysics, 453, 20–43, https://doi.org/10.1016/j.tecto.2007.04.014, 2008.

Basili, R., Kastelic, V., Demircioglu, M. B., Garcia Moreno, D., Nemser, E. S., Petricca, P., Sboras, S. P., Besana-Ostman, G. M., Cabral, J., Camelbeeck, T., Caputo, R., Danciu, L., Domac, H., Fonseca, J. F. de B. D., García-Mayordomo, J., Giardini, D., Glavatovic, B., Gulen, L., Ince, Y., Pavlides, S., Sesetyan, K., Tarabusi, G., Tiberti, M. M., Utkucu, M., Valensise, G., Vanneste, K., Vilanova, S. P., and Wössner, J.: The European Database of Seismogenic Faults (EDSF) compiled in the framework of the Project SHARE. Istituto Nazionale di Geofisica e Vulcanologia (INGV), doi: 10.6092/INGV.IT-SHARE-EDSF., 2013.

Basili, R., Brizuela, B., Herrero, A., Iqbal, S., Lorito, S., Maesano, F. E., Murphy, S., Perfetti, P., Romano, F., Scala, A., Selva, J., Taroni, M., Tiberti, M. M., Thio, H. K., Tonini, R., Volpe, M., Glimsdal, S., Harbitz, C. B., Løvholt, F., Baptista, M. A., Carrilho, F., Matias, L. M., Omira, R., Babeyko, A., Hoechner, A., Gürbüz, M., Pekcan, O., Yalçıner, A., Canals, M., Lastras, G., Agalos, A., Papadopoulos, G., Triantafyllou, I., Benchekroun, S., Agrebi Jaouadi, H., Ben Abdallah, S., Bouallegue, A., Hamdi, H., Oueslati, F., Amato, A., Armigliato, A., Behrens, J., Davies, G., Di Bucci, D., Dolce, M., Geist, E., Gonzalez Vida, J. M., González, M., Macías Sánchez, J., Meletti, C., Ozer Sozdinler, C., Pagani, M., Parsons, T., Polet, J., Power, W., Sørensen, M., and Zaytsev, A.: The Making of the NEAM Tsunami Hazard Model 2018 (NEAMTHM18), Frontiers in Earth Science, 8, https://doi.org/10.3389/feart.2020.616594, 2021.

Basili, R., Danciu, L., Beauval, C., Sesetyan, K., Vilanova, S. P., Adamia, S., Arroucau, P., Atanackov, J., Baize, S., Canora, C., Caputo, R., Carafa, M. M. C., Cushing, M. E., Custódio, S., Demircioglu Tumsa, M. B., Duarte, J. C., Ganas, A., García-Mayordomo, J., Gómez de la Peña, L., Gràcia, E., Jamšek Rupnik, P., Jomard, H., Kastelic, V., Maesano, F. E., Martín-Banda, R., Martínez-Loriente, S., Neres, M., Perea, H., Sket-Motnikar, B., Tiberti, M. M., Tsereteli, N., Tsironi, V., Vallone, R., Vanneste, K., and Zupančič, P.: European Fault-Source Model 2020 (EFSM20): online data on fault geometry and activity parameters, https://doi.org/10.13127/EFSM20, 2022.

Bayat, F., Kowsari, M., and Halldorsson, B.: A new 3-D finite-fault model of the Southwest Iceland bookshelf transform zone, Geophysical Journal International, 231, 1618–1633, https://doi.org/10.1093/gji/ggac272, 2022.

Becker, D. and Meier, T.: Seismic Slip Deficit in the Southwestern Forearc of the Hellenic Subduction Zone, Bulletin of the Seismological Society of America, 100, 325–342, https://doi.org/10.1785/0120090156, 2010.

Bell, R. E., McNeill, L. C., Bull, J. M., Henstock, T. J., Collier, R. E. L., and Leeder, M. R.: Fault architecture, basin structure and evolution of the Gulf of Corinth Rift, central Greece, Basin Research, 21, 824–855, https://doi.org/10.1111/j.1365-2117.2009.00401.x, 2009.

Bergerat, F., Angelier, J., and Villemin, T.: Fault systems and stress patterns on emerged oceanic ridges: a case study in Iceland, Tectonophysics, 179, 183–197, https://doi.org/10.1016/0040-1951(90)90290-O, 1990.

Bilek, S. L. and Lay, T.: Rigidity variations with depth along interplate megathrust faults in subduction zones, Nature, 400, 443–446, https://doi.org/10.1038/22739, 1999.

Bird, P.: An updated digital model of plate boundaries, Geochem. Geophys. Geosyst., 4, https://doi.org/10.1029/2001GC000252, 2003.

Borque, M. J., Sánchez-Alzola, A., Martin-Rojas, I., Alfaro, P., Molina, S., Rosa-Cintas, S., Rodríguez-Caderot, G., Lacy, C., García-Armenteros, J. A., Avilés, M., Herrera-Olmo, A., García-Tortosa, F. J., Estévez, A., and Gil, A. J.: How Much Nubia-Eurasia Convergence Is Accommodated by the NE End of the Eastern Betic Shear Zone (SE Spain)? Constraints From GPS Velocities, Tectonics, 38, 1824–1839, https://doi.org/10.1029/2018TC004970, 2019.

Briole, P., Ganas, A., Elias, P., and Dimitrov, D.: The GPS velocity field of the Aegean. New observations, contribution of the earthquakes, crustal blocks model, Geophysical Journal International, 226, 468–492, https://doi.org/10.1093/gji/ggab089, 2021.

Calais, E., Camelbeeck, T., Stein, S., Liu, M., and Craig, T. J.: A new paradigm for large earthquakes in stable continental plate interiors, Geophys. Res. Lett., 43, https://doi.org/10.1002/2016GL070815, 2016.

Canora, C., Vilanova, S. P., Besana-Ostman, G. M., Carvalho, J., Heleno, S., and Fonseca, J.: The Eastern Lower Tagus Valley Fault Zone in central Portugal: Active faulting in a low-deformation region within a major river environment, Tectonophysics, 660, 117–131, https://doi.org/10.1016/j.tecto.2015.08.026, 2015.

Caputo, R. and Pavlides, S.: Greek Database of Seismogenic Sources (GreDaSS): A compilation of potential seismogenic sources (Mw > 5.5) in the Aegean Region, https://doi.org/10.15160/UNIFE/GREDASS/0200, 2013.

Carafa, M. M. C., Kastelic, V., Bird, P., Maesano, F. E., and Valensise, G.: A "Geodetic Gap" in the Calabrian Arc: Evidence for a Locked Subduction Megathrust?, Geophysical Research Letters, 45, 1794–1804, https://doi.org/10.1002/2017gl076554, 2018.

Civiero, C., Strak, V., Custódio, S., Silveira, G., Rawlinson, N., Arroucau, P., and Corela, C.: A common deep source for upper-mantle upwellings below the Ibero-western Maghreb region from teleseismic P-wave travel-time tomography, Earth and Planetary Science Letters, 499, 157–172, https://doi.org/10.1016/j.epsl.2018.07.024, 2018.

Danciu, L., Şeşetyan, K., Demircioglu, M., Gülen, L., Zare, M., Basili, R., Elias, A., Adamia, S., Tsereteli, N., Yalçın, H., Utkucu, M., Khan, M. A., Sayab, M., Hessami, K., Rovida, A. N., Stucchi, M., Burg, J.-P., Karakhanian, A., Babayan, H., Avanesyan, M., Mammadli, T., Al-Qaryouti, M., Kalafat, D., Varazanashvili, O., Erdik, M., and Giardini, D.: The 2014 Earthquake Model of the Middle East: seismogenic sources, Bulletin of Earthquake Engineering, 16, 3465–3496, https://doi.org/10.1007/s10518-017-0096-8, 2018.

Danciu, L., Nandan, S., Reyes, C., Basili, R., Weatherill, G., Beauval, C., Rovida, A., Vilanova, S., Sesetyan, K., Bard, P.-Y., Cotton, F., Wiemer, S., and Giardini, D.: The 2020 update of the European Seismic Hazard Model: Model Overview. EFEHR Technical Report 001, v1.0.0, 2021.

Danciu, L., Weatherill, G., Rovida, A., Basili, R., Bard, P.-Y., Beauval, C., Nandan, S., Pagani, M., Crowley, H., Sesetyan, K., Villanova, S., Reyes, C., Marti, M., Cotton, F., Wiemer, S., and Giardini, D.: The 2020 European Seismic Hazard Model: Milestones and Lessons Learned, in: Progresses in European Earthquake Engineering and Seismology, edited by: Vacareanu, R. and Ionescu, C., Springer International Publishing, Cham, 3–25, https://doi.org/10.1007/978-3-031-15104-0_1, 2022.

Davies, J. H.: Global map of solid Earth surface heat flow: Global Surface Heat Flow Map, Geochem. Geophys. Geosyst., 14, 4608–4622, https://doi.org/10.1002/ggge.20271, 2013.

Delavaud, E., Cotton, F., Akkar, S., Scherbaum, F., Danciu, L., Beauval, C., Drouet, S., Douglas, J., Basili, R., Sandikkaya, M. A., Segou, M., Faccioli, E., and Theodoulidis, N.: Toward a ground-motion logic tree for probabilistic seismic hazard assessment in Europe, Journal of Seismology, 16, 451–473, https://doi.org/10.1007/s10950-012-9281-z, 2012.

Demircioğlu, M. B., Şeşetyan, K., Duman, T. Y., Çan, T., Tekin, S., and Ergintav, S.: A probabilistic seismic hazard assessment for the Turkish territory: part II—fault source and background seismicity model, Bull Earthquake Eng, 16, 3399–3438, https://doi.org/10.1007/s10518-017-0130-x, 2018.

Devoti, R., Riguzzi, F., Cuffaro, M., and Doglioni, C.: New GPS constraints on the kinematics of the Apennines subduction, Earth and Planetary Science Letters, 273, 163–174, https://doi.org/10.1016/j.epsl.2008.06.031, 2008.

Di Stefano, R., Chiarabba, C., Lucente, F., and Amato, A.: Crustal and uppermost mantle structure in Italy fron the inversion of P-wave arrival times: geodynamic impliations, Geophysical Journal International, 139, 483–498, https://doi.org/10.1046/j.1365-246x.1999.00952.x, 1999.

Diaconescu, M., Craiu, A., Moldovan, I. A., Constantinescu, E. G., and Ghita, C.: Main active faults from eastern part of Romania (Dobrogea and Black Sea). Part II: Transversal and oblique faults system, Romanian Reports in Physics, 71, 708, 2019a.

Diaconescu, M., Craiu, A., Toma-Danila, D., Craiu, G. M., and Ghita, C.: Main active faults from Romania, Part I: Longitudinal and faults system., Romanian Reports in Physics, 71, 702, 2019b.

Diaconescu, M., Craiu, A., Ghita, C., Moldovan, I. A., Oros, E., Constantinescu, E. G., and Marius, M.: Main active faults from Romania. Part III: Fault systems from Dacia tectonic unit, Romanian Reports in Physics, 73, 710, 2021.

DISS Working Group: Database of Individual Seismogenic Sources (DISS), version 3.3.0: A compilation of potential sources for earthquakes larger than M 5.5 in Italy and surrounding areas., 132 Individual Seismogenic Sources, 197 Composite Seismogenic Sources, 38 Debated Seismogenic Sources, 4 Subduction Zones, https://doi.org/10.13127/DISS3.3.0, 2021.

Dutta, R., Jónsson, S., and Vasyura-Bathke, H.: Simultaneous Bayesian Estimation of Non-Planar Fault Geometry and Spatially-Variable Slip, J Geophys Res Solid Earth, 126, https://doi.org/10.1029/2020JB020441, 2021.

Dziewonski, A. M. and Anderson, D. L.: Preliminary reference Earth model, Physics of the Earth and Planetary Interiors, 25, 297–356, https://doi.org/10.1016/0031-9201(81)90046-7, 1981.

Emre, Ö., Duman, T. Y., Özalp, S., Şaroğlu, F., Olgun, Ş., Elmacı, H., and Çan, T.: Active fault database of Turkey, Bull Earthquake Eng, 16, 3229–3275, https://doi.org/10.1007/s10518-016-0041-2, 2018.

England, P. and Jackson, J.: Uncharted seismic risk, Nature Geosci, 4, 348–349, https://doi.org/10.1038/ngeo1168, 2011.

Escartín, J., Cowie, P. A., Searle, R. C., Allerton, S., Mitchell, N. C., MacLeod, C. J., and Slootweg, A. P.: Quantifying tectonic strain and magmatic accretion at a slow spreading ridge segment, Mid-Atlantic Ridge, 29°N, J. Geophys. Res., 104, 10421–10437, https://doi.org/10.1029/1998JB900097, 1999.

Fadil, A., Vernant, P., McClusky, S., Reilinger, R., Gomez, F., Ben Sari, D., Mourabit, T., Feigl, K., and Barazangi, M.: Active tectonics of the western Mediterranean: Geodetic evidence for rollback of a delaminated subcontinental lithospheric slab beneath the Rif Mountains, Morocco, Geol, 34, 529, https://doi.org/10.1130/G22291.1, 2006.

Fernández-Blanco, D., de Gelder, G., Lacassin, R., and Armijo, R.: A new crustal fault formed the modern Corinth Rift, Earth-Science Reviews, 199, 102919, https://doi.org/10.1016/j.earscirev.2019.102919, 2019.

Forslund, T. and Gudmundsson, A.: Crustal spreading due to dikes and faults in southwest Iceland, Journal of Structural Geology, 13, 443–457, https://doi.org/10.1016/0191-8141(91)90017-D, 1991.

Ganas, A.: NOAFAULTS KMZ layer Version 4.0 (V4.0), https://doi.org/10.5281/ZENODO.6326260, 2022.

Ganas, A. and Parsons, T.: Three-dimensional model of Hellenic Arc deformation and origin of the Cretan uplift, J. Geophys. Res., 114, B06404, https://doi.org/10.1029/2008JB005599, 2009.

Ganas, A., Oikonomou, I. A., and Tsimi, C.: NOAfaults: a digital database for active faults in Greece, Bulletin of the Geological Society of Greece, 47, 518–530, https://doi.org/10.12681/bgsg.11079, 2013.

Ganas, A., Tsironi, V., Kollia, E., Delagas, M., Tsimi, C., and Oikonomou, A.: Recent upgrades of the NOA database of active faults in Greece (NOAFAULTs), Proceedings of the 19th General Assembly of WEGENER, Grenoble, France, sciencesconf.org: wegener2018:219400, 2018.

Ganas, A., Briole, P., Bozionelos, G., Barberopoulou, A., Elias, P., Tsironi, V., Valkaniotis, S., Moshou, A., and Mintourakis, I.: The 25 October 2018 Mw = 6.7 Zakynthos earthquake (Ionian Sea, Greece): A low-angle fault model based on GNSS data, relocated seismicity, small tsunami and implications for the seismic hazard in the west Hellenic Arc, Journal of Geodynamics, 137, 101731, https://doi.org/10.1016/j.jog.2020.101731, 2020.

Garcia, S., Angelier, J., Bergerat, F., and Homberg, C.: Tectonic analysis of an oceanic transform fault zone based on fault-slip data and earthquake focal mechanisms: the Húsavík–Flatey Fault zone, Iceland, Tectonophysics, 344, 157–174, https://doi.org/10.1016/S0040-1951(01)00282-7, 2002.

García-Mayordomo, J., Insua-Arévalo, J. M., Martínez-Díaz, J. J., Jiménez-Díaz, A., Martín-Banda, R., Martín-Alfageme, S., Álvarez-Gómez, J. A., Rodríguez-Peces, M., Pérez-López, R., Rodríguez-Pascua, M. A., Masana, E., Perea, H., Martín-González, F., Giner-Robles, J., Nemser, E. S., and Cabral, J.: The Quaternary Active Faults Database of Iberia (QAFI v.2.0), Journal of Iberian Geology, 38, 285–302, https://doi.org/10.5209/rev_JIGE.2012.v38.n1.39219, 2012.

García-Mayordomo, J., Martín-Banda, R., Insua-Arévalo, J. M., Álvarez-Gómez, J. A., Martínez-Díaz, J. J., and Cabral, J.: Active fault databases: building a bridge between earthquake geologists and seismic hazard practitioners, the case of the QAFI v.3 database, Nat. Hazards Earth Syst. Sci., 17, 1447–1459, https://doi.org/10.5194/nhess-17-1447-2017, 2017.

Geist, E. L. and Bilek, S. L.: Effect of depth-dependent shear modulus on tsunami generation along subduction zones, Geophys. Res. Lett., 28, 1315–1318, https://doi.org/10.1029/2000GL012385, 2001.

Goes, S., Agrusta, R., Van Hunen, J., and Garel, F.: Subduction-transition zone interaction: A review, Geosphere, 13, 644–664, https://doi.org/10.1130/GES01476.1, 2017.

Gold, R. D., Friedrich, A., Kübler, S., and Salamon, M.: Apparent Late Quaternary Fault-Slip Rate Increase in the Southern Lower Rhine Graben, Central Europe, Bulletin of the Seismological Society of America, 107, 563–580, https://doi.org/10.1785/0120160197, 2017.

Gómez de la Peña, L., Ranero, C. R., and Gràcia, E.: The Crustal Domains of the Alboran Basin (Western Mediterranean), Tectonics, 37, 3352–3377, https://doi.org/10.1029/2017TC004946, 2018.

Gómez de la Peña, L., Gràcia, E., Maesano, F. E., Basili, R., Kopp, H., Sánchez-Serra, C., Scala, A., Romano, F., Volpe, M., Piatanesi, A., and R. Ranero, C.: A first appraisal of the seismogenic and tsunamigenic potential of the largest fault systems in the westernmost Mediterranean, Marine Geology, 445, https://doi.org/10.1016/j.margeo.2022.106749, 2022.

Gomez, F., Barazangi, M., and Bensaid, M.: Active tectonism in the intracontinental Middle Atlas Mountains of Morocco: synchronous crustal shortening and extension, Journal of the Geological Society, 153, 389–402, https://doi.org/10.1144/gsjgs.153.3.0389, 1996.

Gómez-Novell, O., García-Mayordomo, J., Ortuño, M., Masana, E., and Chartier, T.: Fault System-Based Probabilistic Seismic Hazard Assessment of a Moderate Seismicity Region: The Eastern Betics Shear Zone (SE Spain), Front. Earth Sci., 8, 579398, https://doi.org/10.3389/feart.2020.579398, 2020a.

Gómez-Novell, O., Chartier, T., García-Mayordomo, J., Ortuño, M., Masana, E., Insua-Arévalo, J. M., and Scotti, O.: Modelling earthquake rupture rates in fault systems for seismic hazard assessment: The Eastern Betics Shear Zone, Engineering Geology, 265, 105452, https://doi.org/10.1016/j.enggeo.2019.105452, 2020b.

Grad, M., Tiira, T., and ESC Working Group: The Moho depth map of the European Plate, Geophysical Journal International, 176, 279–292, https://doi.org/10.1111/j.1365-246X.2008.03919.x, 2009.

Grützner, C., Carson, E., Walker, R. T., Rhodes, E. J., Mukambayev, A., Mackenzie, D., Elliott, J. R., Campbell, G., and Abdrakhmatov, K.: Assessing the activity of faults in continental interiors: Palaeoseismic insights from SE Kazakhstan, Earth and Planetary Science Letters, 459, 93–104, https://doi.org/10.1016/j.epsl.2016.11.025, 2017.

Gutscher, M.-A., Roger, J., Baptista, M.-A., Miranda, J. M., and Tinti, S.: Source of the 1693 Catania earthquake and tsunami (southern Italy): New evidence from tsunami modeling of a locked subduction fault plane, Geophys. Res. Lett., 33, L08309, https://doi.org/10.1029/2005GL025442, 2006.

Gutscher, M.-A., Dominguez, S., Westbrook, G. K., and Leroy, P.: Deep structure, recent deformation and analog modeling of the Gulf of Cadiz accretionary wedge: Implications for the 1755 Lisbon earthquake, Tectonophysics, 475, 85–97, https://doi.org/10.1016/j.tecto.2008.11.031, 2009.

Halpaap, F., Rondenay, S., and Ottemöller, L.: Seismicity, Deformation, and Metamorphism in the Western Hellenic Subduction Zone: New Constraints From Tomography, J. Geophys. Res. Solid Earth, 123, 3000–3026, https://doi.org/10.1002/2017JB015154, 2018.

Halpaap, F., Rondenay, S., Perrin, A., Goes, S., Ottemöller, L., Austrheim, H., Shaw, R., and Eeken, T.: Earthquakes track subduction fluids from slab source to mantle wedge sink, Sci. Adv., 5, eaav7369, https://doi.org/10.1126/sciadv.aav7369, 2019.

Haslinger, F., Basili, R., Bossu, R., Cauzzi, C., Cotton, F., Crowley, H., Custódio, S., Danciu, L., Locati, M., Michelini, A., Molinari, I., Ottemöller, L., and Parolai, S.: Coordinated and Interoperable Seismological Data and Product Services in Europe: the EPOS Thematic Core Service for Seismology, Annals of Geophysics, 65, https://doi.org/10.4401/ag-8767, 2022.

Hayes, G. P., Moore, G. L., Portner, D. E., Hearne, M., Flamme, H., Furtney, M., and Smoczyk, G. M.: Slab2, a comprehensive subduction zone geometry model, Science, 362, 58–61, https://doi.org/10.1126/science.aat4723, 2018.

Herrero-Barbero, P., Álvarez-Gómez, J. A., Martínez-Díaz, J. J., and Klimowitz, J.: Neogene Basin Inversion and Recent Slip Rate Distribution of the Northern Termination of the Alhama de Murcia Fault (Eastern Betic Shear Zone, SE Spain), Tectonics, 39, https://doi.org/10.1029/2019TC005750, 2020.

Heuret, A., Lallemand, S., Funiciello, F., Piromallo, C., and Faccenna, C.: Physical characteristics of subduction interface type

795     seismogenic zones revisited, Geochem. Geophys. Geosyst., 12, n/a-n/a, https://doi.org/10.1029/2010GC003230, 2011.

Hollenstein, Ch., Müller, M. D., Geiger, A., and Kahle, H.-G.: Crustal motion and deformation in Greece from a decade of GPS measurements, 1993–2003, Tectonophysics, 449, 17–40, https://doi.org/10.1016/j.tecto.2007.12.006, 2008.

Howell, A., Jackson, J., Copley, A., McKenzie, D., and Nissen, E.: Subduction and vertical coastal motions in the eastern Mediterranean, Geophysical Journal International, 211, 593–620, https://doi.org/10.1093/gji/ggx307, 2017.

800     IGME: QAFI v.3: Quaternary Faults Database of Iberia, 2015.

ISC: On-line Bulletin, International Seismological Centre, 2019.

Johnston, A. C.: Seismotectonic interpretations and conclusions from the stable continental region seismicity database, Electric Power Research Institute, Palo Alto, California, 1994.

Jomard, H., Cushing, E. M., Palumbo, L., Baize, S., David, C., and Chartier, T.: Transposing an active fault database into a

805     seismic hazard fault model for nuclear facilities – Part 1: Building a database of potentially active faults (BDFA) for metropolitan France, Nat. Hazards Earth Syst. Sci., 17, 1573–1584, https://doi.org/10.5194/nhess-17-1573-2017, 2017.

Kagan, Y. Y. and Jackson, D. D.: Tohoku Earthquake: A Surprise?, Bulletin of the Seismological Society of America, 103, 1181–1194, https://doi.org/10.1785/0120120110, 2013.

Kagan, Y. Y., Bird, P., and Jackson, D. D.: Earthquake Patterns in Diverse Tectonic Zones of the Globe, Pure Appl. Geophys.,

810     167, 721–741, https://doi.org/10.1007/s00024-010-0075-3, 2010.

Kastens, K. A.: Rate of outward growth of the Mediterranean ridge accretionary complex, Tectonophysics, 199, 25–50, https://doi.org/10.1016/0040-1951(91)90117-B, 1991.

Koulali, A., Ouazar, D., Tahayt, A., King, R. W., Vernant, P., Reilinger, R. E., McClusky, S., Mourabit, T., Davila, J. M., and Amraoui, N.: New GPS constraints on active deformation along the Africa–Iberia plate boundary, Earth and Planetary Science

815     Letters, 308, 211–217, https://doi.org/10.1016/j.epsl.2011.05.048, 2011.

LaFemina, P. C., Dixon, T. H., Malservisi, R., Árnadóttir, T., Sturkell, E., Sigmundsson, F., and Einarsson, P.: Geodetic GPS measurements in south Iceland: Strain accumulation and partitioning in a propagating ridge system, J. Geophys. Res., 110, https://doi.org/10.1029/2005JB003675, 2005.

Laigle, M., Hirn, A., Sachpazi, M., and Clément, C.: Seismic coupling and structure of the Hellenic subduction zone in the

820     Ionian Islands region, Earth and Planetary Science Letters, 200, 243–253, https://doi.org/10.1016/S0012-821X(02)00654-4, 2002.

Laigle, M., Sachpazi, M., and Hirn, A.: Variation of seismic coupling with slab detachment and upper plate structure along the western Hellenic subduction zone, Tectonophysics, 391, 85–95, https://doi.org/10.1016/j.tecto.2004.07.009, 2004.

Leonard, M.: Earthquake Fault Scaling: Self-Consistent Relating of Rupture Length, Width, Average Displacement, and

825     Moment Release, Bulletin of the Seismological Society of America, 100, 1971–1988, https://doi.org/10.1785/0120090189, 2010.

Leonard, M.: Self-Consistent Earthquake Fault-Scaling Relations: Update and Extension to Stable Continental Strike-Slip Faults, Bulletin of the Seismological Society of America, 104, 2953–2965, https://doi.org/10.1785/0120140087, 2014.

MacDonald, K. C. and Luyendyk, B. P.: Deep-tow studies of the structure of the Mid-Atlantic Ridge crest near lat 37°N, GSA Bulletin, 88, 621–636, https://doi.org/10.1130/0016-7606(1977)88<621:DSOTSO>2.0.CO;2, 1977.

Maesano, F. E., Tiberti, M. M., and Basili, R.: The Calabrian Arc: Three-dimensional modelling of the subduction interface, Scientific Reports, 7, https://doi.org/10.1038/s41598-017-09074-8, 2017.

Maesano, F. E., Buttinelli, M., Maffucci, R., Toscani, G., Basili, R., Bonini, L., Burrato, P., Fedorik, J., Fracassi, U., Panara, Y., Tarabusi, G., Tiberti, M. M., Valensise, G., Vallone, R., and Vannoli, P.: Buried alive: imaging the November 9, 2022, Mw 5.5 earthquake source on the offshore Adriatic blind thrust front of the Northern Apennines (Italy)., Geophysical Research Letters, https://doi.org/10.1029/2022GL102299, 2023.

Maggini, M. and Caputo, R.: Rheological behaviour in continental and oceanic subduction:inferences for the seismotectonics of the Aegean Region, Turkish J Earth Sci, https://doi.org/10.3906/yer-1909-4, 2020.

Maggini, M. and Caputo, R.: Seismological data versus rheological modelling: Comparisons across the Aegean Region for improving the seismic hazard assessment, Journal of Structural Geology, 145, 104312, https://doi.org/10.1016/j.jsg.2021.104312, 2021.

Martínez-Loriente, S., Gràcia, E., Bartolome, R., Sallarès, V., Connors, C., Perea, H., Lo Iacono, C., Klaeschen, D., Terrinha, P., Dañobeitia, J. J., and Zitellini, N.: Active deformation in old oceanic lithosphere and significance for earthquake hazard: Seismic imaging of the Coral Patch Ridge area and neighboring abyssal plains (SW Iberian Margin), Geochem. Geophys. Geosyst., 14, 2206–2231, https://doi.org/10.1002/ggge.20173, 2013.

Martínez-Loriente, S., Sallarès, V., Gràcia, E., Bartolome, R., Dañobeitia, J. J., and Zitellini, N.: Seismic and gravity constraints on the nature of the basement in the Africa-Eurasia plate boundary: New insights for the geodynamic evolution of the SW Iberian margin: Thin oceanic crust at the CPR and SH, J. Geophys. Res. Solid Earth, 119, 127–149, https://doi.org/10.1002/2013JB010476, 2014.

Martínez-Loriente, S., Gràcia, E., Bartolome, R., Perea, H., Klaeschen, D., Dañobeitia, J. J., Zitellini, N., Wynn, R. B., and Masson, D. G.: Morphostructure, tectono-sedimentary evolution and seismic potential of the Horseshoe Fault, SW Iberian Margin, Basin Res, 30, 382–400, https://doi.org/10.1111/bre.12225, 2018.

Morell, K. D., Styron, R., Stirling, M., Griffin, J., Archuleta, R., and Onur, T.: Seismic Hazard Analyses From Geologic and Geomorphic Data: Current and Future Challenges, Tectonics, 39, https://doi.org/10.1029/2018TC005365, 2020.

Müller, R. D., Sdrolias, M., Gaina, C., and Roest, W. R.: Age, spreading rates, and spreading asymmetry of the world's ocean crust, Geochem. Geophys. Geosyst., 9, n/a-n/a, https://doi.org/10.1029/2007GC001743, 2008.

Neres, M., Carafa, M. M. C., Fernandes, R. M. S., Matias, L., Duarte, J. C., Barba, S., and Terrinha, P.: Lithospheric deformation in the Africa-Iberia plate boundary: Improved neotectonic modeling testing a basal-driven Alboran plate, J. Geophys. Res. Solid Earth, 121, 6566–6596, https://doi.org/10.1002/2016JB013012, 2016.

860     Nijholt, N., Govers, R., and Wortel, R.: On the forces that drive and resist deformation of the south-central Mediterranean: a mechanical model study, Geophysical Journal International, 214, 876–894, https://doi.org/10.1093/gji/ggy144, 2018.

NOAA National Geophysical Data Center: ETOPO1 1 arc-minute global relief model. NOAA National Centers for Environmental Information., 2009.

Nocquet, J.-M.: Present-day kinematics of the Mediterranean: A comprehensive overview of GPS results, Tectonophysics,
865     579, 220–242, https://doi.org/10.1016/j.tecto.2012.03.037, 2012.

Onur, T., Gok, R., Godoladze, T., Gunia, I., Boichenko, G., Buzaladze, A., Tumanova, N., Dzmanashvili, M., Sukhishvili, L., Javakishvili, Z., Cowgill, E., Bondar, I., and Yetirmishli, G.: Probabilistic Seismic Hazard Assessment for Georgia, https://doi.org/10.2172/1511856, 2019.

Onur, T., Gok, R., Godoladze, T., Gunia, I., Boichenko, G., Buzaladze, A., Tumanova, N., Dzmanashvili, M., Sukhishvili, L.,
870     Javakishvili, Z., Cowgill, E., Bondár, I., and Yetirmishli, G.: Probabilistic Seismic Hazard Assessment Using Legacy Data in Georgia, Seismological Research Letters, 91, 1500–1517, https://doi.org/10.1785/0220190331, 2020.

Pagani, M., Monelli, D., Weatherill, G., Danciu, L., Crowley, H., Silva, V., Henshaw, P., Butler, L., Nastasi, M., Panzeri, L., Simionato, M., and Vigano, D.: OpenQuake Engine: An Open Hazard (and Risk) Software for the Global Earthquake Model, Seismological Research Letters, 85, 692–702, https://doi.org/10.1785/0220130087, 2014.

875     Palano, M., González, P. J., and Fernández, J.: The Diffuse Plate boundary of Nubia and Iberia in the Western Mediterranean: Crustal deformation evidence for viscous coupling and fragmented lithosphere, Earth and Planetary Science Letters, 430, 439–447, https://doi.org/10.1016/j.epsl.2015.08.040, 2015.

Panara, Y., Maesano, F. E., Amadori, C., Fedorik, J., Toscani, G., and Basili, R.: Probabilistic Assessment of Slip Rates and Their Variability Over Time of Offshore Buried Thrusts: A Case Study in the Northern Adriatic Sea, Frontiers in Earth Science,
880     9, https://doi.org/10.3389/feart.2021.664288, 2021.

Passone, L. and Mai, P. M.: Kinematic Earthquake Ground-Motion Simulations on Listric Normal Faults, Bulletin of the Seismological Society of America, 107, 2980–2993, https://doi.org/10.1785/0120170111, 2017.

Pastor, A., Babault, J., Owen, L. A., Teixell, A., and Arboleya, M.-L.: Extracting dynamic topography from river profiles and cosmogenic nuclide geochronology in the Middle Atlas and the High Plateaus of Morocco, Tectonophysics, 663, 95–109,
885     https://doi.org/10.1016/j.tecto.2015.06.007, 2015.

Perea, H., Gràcia, E., Martínez-Loriente, S., Bartolome, R., de la Peña, L. G., de Mol, B., Moreno, X., Iacono, C. L., Diez, S., Tello, O., Gómez-Ballesteros, M., and Dañobeitia, J. J.: Kinematic analysis of secondary faults within a distributed shear-zone reveals fault linkage and increased seismic hazard, Marine Geology, 399, 23–33, https://doi.org/10.1016/j.margeo.2018.02.002, 2018.

890     Perea, H., Martínez-Loriente, S., Maloney, J., Maesano, F. E., and Vannucchi, P.: Editorial: Submarine Active Faults: From Regional Observations to Seismic Hazard Characterization, Front. Earth Sci., 9, 809205, https://doi.org/10.3389/feart.2021.809205, 2021.

Reilinger, R., McClusky, S., Vernant, P., Lawrence, S., Ergintav, S., Cakmak, R., Ozener, H., Kadirov, F., Guliev, I., Stepanyan, R., Nadariya, M., Hahubia, G., Mahmoud, S., Sakr, K., ArRajehi, A., Paradissis, D., Al-Aydrus, A., Prilepin, M., Guseva, T., Evren, E., Dmitrotsa, A., Filikov, S. V., Gomez, F., Al-Ghazzi, R., and Karam, G.: GPS constraints on continental deformation in the Africa-Arabia-Eurasia continental collision zone and implications for the dynamics of plate interactions, J. Geophys. Res., 111, n/a-n/a, https://doi.org/10.1029/2005JB004051, 2006.

Reilinger, R., McClusky, S., Paradissis, D., Ergintav, S., and Vernant, P.: Geodetic constraints on the tectonic evolution of the Aegean region and strain accumulation along the Hellenic subduction zone, Tectonophysics, 488, 22–30, https://doi.org/10.1016/j.tecto.2009.05.027, 2010.

Rigby, M.: Recent faulting and active shortening of the Middle Atlas Mountains, Morocco, within the diffuse African-Eurasian plate boundary, Master of Science Degree Thesis, Faculty of the Graduate School, University of Missouri-Columbia, 2008.

Rögnvaldsson, S. T., Gudmundsson, A., and Slunga, R.: Seismotectonic analysis of the Tjörnes Fracture Zone, an active transform fault in north Iceland, J. Geophys. Res., 103, 30117–30129, https://doi.org/10.1029/98JB02789, 1998.

Rontogianni, S.: Comparison of geodetic and seismic strain rates in Greece by using a uniform processing approach to campaign GPS measurements over the interval 1994–2000, Journal of Geodynamics, 50, 381–399, https://doi.org/10.1016/j.jog.2010.04.008, 2010.

Rust, D. and Whitworth, M.: A unique ~12 ka subaerial record of rift-transform triple-junction tectonics, NE Iceland, Sci Rep, 9, 9669, https://doi.org/10.1038/s41598-019-45903-8, 2019.

Sachpazi, M., Laigle, M., Charalampakis, M., Diaz, J., Kissling, E., Gesret, A., Becel, A., Flueh, E., Miles, P., and Hirn, A.: Segmented Hellenic slab rollback driving Aegean deformation and seismicity, Geophys. Res. Lett., 43, 651–658, https://doi.org/10.1002/2015GL066818, 2016.

Sallarès, V. and Ranero, C. R.: Upper-plate rigidity determines depth-varying rupture behaviour of megathrust earthquakes, Nature, 576, 96–101, https://doi.org/10.1038/s41586-019-1784-0, 2019.

Sallarès, V., Gailler, A., Gutscher, M.-A., Graindorge, D., Bartolomé, R., Gràcia, E., Díaz, J., Dañobeitia, J. J., and Zitellini, N.: Seismic evidence for the presence of Jurassic oceanic crust in the central Gulf of Cadiz (SW Iberian margin), Earth and Planetary Science Letters, 311, 112–123, https://doi.org/10.1016/j.epsl.2011.09.003, 2011.

Sallarès, V., Martínez-Loriente, S., Prada, M., Gràcia, E., Ranero, C., Gutscher, M.-A., Bartolome, R., Gailler, A., Dañobeitia, J. J., and Zitellini, N.: Seismic evidence of exhumed mantle rock basement at the Gorringe Bank and the adjacent Horseshoe and Tagus abyssal plains (SW Iberia), Earth and Planetary Science Letters, 365, 120–131, https://doi.org/10.1016/j.epsl.2013.01.021, 2013.

Sanz de Galdeano, C., Azañón, J. M., Cabral, J., Ruano, P., Alfaro, P., Canora, C., Ferrater, M., García Tortosa, F. J., García-Mayordomo, J., Gràcia, E., Insua-Arévalo, J. M., Jiménez Bonilla, A., Lacan, P. G., Marín-Lechado, C., Martín-Banda, R., Martín González, F., Martínez-Díaz, J. J., Martín-Rojas, I., Masana, E., Ortuño, M., Pedrera, A., Perea, H., and Simón, J. L.: Active Faults in Iberia, in: The Geology of Iberia: A Geodynamic Approach, edited by: Quesada, C. and Oliveira, J. T., Springer International Publishing, Cham, 33–75, https://doi.org/10.1007/978-3-030-10931-8_4, 2020.

Satake, K. and Tanioka, Y.: Sources of Tsunami and Tsunamigenic Earthquakes in Subduction Zones, Pure and Applied Geophysics, 154, 467–483, https://doi.org/10.1007/s000240050240, 1999.

Scala, A., Lorito, S., Romano, F., Murphy, S., Selva, J., Basili, R., Babeyko, A., Herrero, A., Hoechner, A., Løvholt, F.,

930    Maesano, F. E., Perfetti, P., Tiberti, M. M., Tonini, R., Volpe, M., Davies, G., Festa, G., Power, W., Piatanesi, A., and Cirella, A.: Effect of Shallow Slip Amplification Uncertainty on Probabilistic Tsunami Hazard Analysis in Subduction Zones: Use of Long-Term Balanced Stochastic Slip Models, Pure and Applied Geophysics, 177, 1497–1520, https://doi.org/10.1007/s00024-019-02260-x, 2020.

Serra, C. S., Martínez-Loriente, S., Gràcia, E., Urgeles, R., Gómez de la Peña, L., Maesano, F. E., Basili, R., Volpe, M.,

935    Romano, F., Scala, A., Piatanesi, A., and Lorito, S.: Sensitivity of Tsunami Scenarios to Complex Fault Geometry and Heterogeneous Slip Distribution: Case-Studies for SW Iberia and NW Morocco, Journal of Geophysical Research: Solid Earth, 126, https://doi.org/10.1029/2021JB022127, 2021.

Shaw, B. and Jackson, J.: Earthquake mechanisms and active tectonics of the Hellenic subduction zone, Geophysical Journal International, https://doi.org/10.1111/j.1365-246X.2010.04551.x, 2010.

940    Skarlatoudis, A. A., Somerville, P. G., and Thio, H. K.: Source-Scaling Relations of Interface Subduction Earthquakes for Strong Ground Motion and Tsunami Simulation, Bulletin of the Seismological Society of America, 106, 1652–1662, https://doi.org/10.1785/0120150320, 2016.

Šket Motnikar, B., Zupančič, P., Živčić, M., Atanackov, J., Jamšek Rupnik, P., Čarman, M., Danciu, L., and Gosar, A.: The 2021 seismic hazard model for Slovenia (SHMS21): overview and results, Bull Earthquake Eng, 20, 4865–4894,

945    https://doi.org/10.1007/s10518-022-01399-8, 2022.

Stich, D., Serpelloni, E., de Lis Mancilla, F., and Morales, J.: Kinematics of the Iberia–Maghreb plate contact from seismic moment tensors and GPS observations, Tectonophysics, 426, 295–317, https://doi.org/10.1016/j.tecto.2006.08.004, 2006.

Styron, R. and Pagani, M.: The GEM Global Active Faults Database, Earthquake Spectra, 36, 160–180, https://doi.org/10.1177/8755293020944182, 2020.

950    Syracuse, E. M., van Keken, P. E., and Abers, G. A.: The global range of subduction zone thermal models, Physics of the Earth and Planetary Interiors, 183, 73–90, https://doi.org/10.1016/j.pepi.2010.02.004, 2010.

Thiebot, E. and Gutscher, M.-A.: The Gibraltar Arc seismogenic zone (part 1): Constraints on a shallow east dipping fault plane source for the 1755 Lisbon earthquake provided by seismic data, gravity and thermal modeling, Tectonophysics, 426, 135–152, https://doi.org/10.1016/j.tecto.2006.02.024, 2006.

955    Thingbaijam, K. K. S., Martin Mai, P., and Goda, K.: New Empirical Earthquake Source-Scaling Laws, Bulletin of the Seismological Society of America, 107, 2225–2246, https://doi.org/10.1785/0120170017, 2017.

Tonini, R., Basili, R., Maesano, F. E., Tiberti, M. M., Lorito, S., Romano, F., Scala, A., and Volpe, M.: Importance of earthquake rupture geometry on tsunami modelling: The Calabrian Arc subduction interface (Italy) case study, Geophysical Journal International, 223, 1805–1819, https://doi.org/10.1093/gji/ggaa409, 2020.

960    Vanneste, K., Camelbeeck, T., and Verbeeck, K.: A Model of Composite Seismic Sources for the Lower Rhine Graben, Northwest Europe, Bulletin of the Seismological Society of America, 103, 984–1007, https://doi.org/10.1785/0120120037, 2013.

Wang, K. and Dixon, T.: "Coupling" Semantics and science in earthquake research, Eos Trans. AGU, 85, 180, https://doi.org/10.1029/2004EO180005, 2004.

965    Wdowinski, S., Ben-Avraham, Z., Arvidsson, R., and Ekström, G.: Seismotectonics of the Cyprian Arc, Geophysical Journal International, 164, 176–181, https://doi.org/10.1111/j.1365-246X.2005.02737.x, 2006.

Wells, D. L. and Coppersmith, K. J.: New empirical relationships among magnitude, rupture length, rupture width, rupture area, and surface displacement, Bulletin of the Seismological Society of America, 84, 974–1002, https://doi.org/10.1785/BSSA0840040974, 1994.

970    van der Woerd, J., Dorbath, C., Ousadou, F., Dorbath, L., Delouis, B., Jacques, E., Tapponnier, P., Hahou, Y., Menzhi, M., Frogneux, M., and Haessler, H.: The Al Hoceima Mw 6.4 earthquake of 24 February 2004 and its aftershocks sequence, Journal of Geodynamics, 77, 89–109, https://doi.org/10.1016/j.jog.2013.12.004, 2014.

Woessner, J., Danciu, L., Giardini, D., Crowley, H., Cotton, F., Grünthal, G., Valensise, G., Arvidsson, R., Basili, R., Demircioglu, M. B., Hiemer, S., Meletti, C., Musson, R. W., Rovida, A. N., Sesetyan, K., Stucchi, M., Anastasiadis, A., Akkar,

975    S., Engin Bal, I., Barba, S., Bard, P.-Y., Beauval, C., Bolliger, M., Bosse, C., Bonjour, C., Bungum, H., Carafa, M., Cameelbeeck, T., Carvalho, A., Campos-Costa, A., Coelho, E., Colombi, M., D'amico, V., Devoti, R., Drouet, S., Douglas, J., Edwards, B., Erdik, M., Fäh, D., Fonseca, J., Fotopoulou, S., Glavatovic, B., Gómez Capera, A. A., Hauser, J., Husson, F., Kastelic, V., Kästli, P., Karatzetzou, A., Kaviris, G., Keller, N., Kierulf, H. P., Kouskouna, V., Krishnamurty, R., Lang, D., Lemoine, A., Lindholm, C., Makropoulos, K., Manakou, M., Marmureanu, G., Martinelli, F., Garcia Mayordomo, J.,

980    Mihaljevic, J., Monelli, D., Garcia-Moreno, D., Nemser, E., Pagani, M., Pinho, R., Pisani, A. R., Pitilakis, D., Pitilakis, K., Poggi, V., Radulian, M., Riga, E., Sandikkaya, M. A., Segou, M., Siegert, R., Silva, V., Stromeyer, D., Sousa, L., Sørensen, M. B., Tellez-Arenas, A., Vanneste, K., Wahlstöm, R., Weatherill, G., Viganò, D., Vilanova, S., Yenier, E., Zulfikar, C., Adams, J., Bommer, J. J., Bonilla, F., Faccioli, E., Gülen, L., Koller, M., Pinto, A., Pinto, P., Papaioannou, C., Peruzza, L., Scherbaum, F., et al.: The 2013 European Seismic Hazard Model: key components and results, Bulletin of Earthquake

985    Engineering, 13, 3553–3596, https://doi.org/10.1007/s10518-015-9795-1, 2015.

## Appendix A

**Table A1 Files distributed for download (GeoJSON files, ESRI shapefiles, MapInfo tables) and via OGC WFS. The rightmost column indicates the relevant Table number with the attribute descriptions provided below in this Appendix.**

| Category | File name | Description | Parameters table link. |
|---|---|---|---|
| Crustal Faults (CF) | EFSM20_CF_TOP | Trace of the fault plane upper edge. Polylines. | A3 |
| | EFSM20_CF_BOT | Trace of the fault plane lower edge. Polylines. | A3 |
| | EFSM20_CF_MID | Trace of the fault plane middle line. Polylines. | A3 |
| | EFSM20_CF_PLD | Vertical projection of the inclined fault planes (in the local dip direction along strike) onto the ground surface. Polygons. | A3 |
| | EFSM20_CFDepths | Depth isolines (contours) of the fault planes, including top e bottom. Polylines. | A4 |
| Subduction Systems (SS) | EFSM20_SlabDepths | Depth isolines (contours) representing the geometry of the top surface of the slab. Polylines. | A5 |
| | EFSM20_SI_Parameters | Subduction Interface (SI) parameters. Polygons encompassing the SI area in map view. | A6 |
| | EFSM20_SI_Discretization | Subduction Interface (SI) discretized in areas spanning 1 km depth. Polygons encompassing each area in map view. | A7 |
| | EFSM20_SI_Realizations | Subduction Interface (SI) model realizations considering uncertainties. Polygons encompassing each area of the different realizations in map view. | A8 |
| | EFSM20_IS_Lattice | Intraslab (IS) model constituted by equally-spaced nodes sampling the crustal part of the slab volume. Points. | A9 |

990     **Table A2 Files distributed via OGC WMS only.**

| Category | File name | Description |
|---|---|---|
| Crustal Faults (CF) | EFSM20_CFDepths ColorScaleCFDepths.sld | Color-coded depth isolines of the fault planes, including the top and bottom. The spacing interval is 0.5 km. |
| | EFSM20_CF_FaultTypes ColorScaleFaultTypes.sld | Color-coded fault types: normal, reverse, right-lateral, left-lateral. |
| | EFSM20_CF_SlipRates ColorScaleSR.sld | Color-coded slip rates. Log-linear separation scale. Four different layers for minimum, maximum, arithmetic mean (default), and geometric mean. |
| | EFSM20_CF_MaxMagnitude ColorScaleMw02.sld | Color-coded maximum magnitude. Five different layers for the average (default), and the 2nd, 5th, 95th, and 98th percentiles. |
| | EFSM20_CF_MomentRates ColorScaleM0R.sld | Color-coded moment rates. Log scale. Four different layers for minimum, maximum, arithmetic mean (default), and geometric mean. |
| Subduction Systems (SS) | EFSM20_SlabDepths ColorScaleSlabDepths.sld | Color-coded depth isolines of the top surface of the slab. Spacing interval is 1 km between 0-40 km and 10 km between 40-300 km. |

**Table A3 Definition of the crustal fault attributes. These attributes are the same for EFSM20_CF_TOP, EFSM20_CF_BOT, EFSM20_CF_MID, and EFSM20_CF_PLD files, in any of the distributed format or WFS service.**

| Field | Variable | Units | Description |
|---|---|---|---|
| IDFS | Char(7) | n.a. | Identifier of the fault source within EFSM20. |
| IDDS | Char(3) | n.a. | Number of the dataset linked to the file "DescriptionOfDatasets". |
| IDSource | Char(24) | n.a. | Identifier given in the original source, if available. |
| StrikeMin | Float | degrees | The minimum value of the fault orientation, between 0-360° increasing clockwise from the north following the right-hand rule. Recalculated from the reshaped fault trace. Rounded to the nearest integer. |
| StrikeAvg | Float | degrees | The average value of the fault orientation, between 0-360° increasing clockwise from the north following the right-hand rule. Recalculated from the reshaped fault trace. Rounded to the nearest integer. |
| StrikeMax | Float | degrees | The maximum value of the fault orientation, between 0-360° increasing clockwise from the north following the right-hand rule. Recalculated from the reshaped fault trace. Rounded to the nearest integer. |
| DipMin | Float | degrees | Minimum value of the dip angle, between 0-90° increasing downward from the horizontal. Rounded to the nearest integer. |
| DipAvg | Float | degrees | Average value of the dip angle, between 0-90° increasing downward from the horizontal. Rounded to the nearest integer. |
| DipMax | Float | degrees | Maximum value of the dip angle, between 0-90° increasing downward from the horizontal. Rounded to the nearest integer. |
| RakeMin | Float | degrees | Minimum value of the hanging-wall sense of movement between -180-180° increasing counterclockwise from the horizontal. Rounded to the nearest integer. |
| RakeAvg | Float | degrees | Average value of the hanging-wall sense of movement between -180-180° increasing counterclockwise from the horizontal. Rounded to the nearest integer. |
| RakeMax | Float | degrees | Maximum value of the hanging-wall sense of movement between -180-180° increasing counterclockwise from the horizontal. Rounded to the nearest integer. |
| MinDepth | Float | km | Value of the minimum depth of the fault, or depth of the upper edge, positive downward from sea level. Rounded to the half kilometer. |
| MaxDepth | Float | km | Value of the maximum depth of the fault, or depth of the lower edge, positive downward from sea level. Rounded to the half kilometer. |
| Length | Float | km | Length of the fault measured along the trace of the upper edge. Rounded to the 1st decimal. |
| E2ELength | Float | km | End-to-end length of the fault, corresponding to the shortest distance between the farthest endpoints on the trace of the upper edge. Rounded to the 1st decimal. |
| WidthMin | Float | km | Minimum value of the fault width, measured along the dip direction, as calculated from depth and maximum dip. Rounded to the 1st decimal. |
| WidthAvg | Float | km | Average value of the fault width, measured along the dip direction, as calculated from depth and average dip. Rounded to the 1st decimal. |
| WidthMax | Float | km | Maximum value of the fault width, measured along the dip direction, as calculated from depth and minimum dip. Rounded to the 1st decimal. |

| | | | |
|---|---|---|---|
| AreaMin | Float | km^2 | Minimum value of the fault area obtained by multiplying total length by width. Rounded to the nearest integer. |
| AreaAvg | Float | km^2 | Average value of the fault area obtained by multiplying total length by width. Rounded to the nearest integer. |
| AreaMax | Float | km^2 | Maximum value of the fault area obtained by multiplying total length by width. Rounded to the nearest integer. |
| SRMin | Float | mm/yr | Minimum value of the slip rate in mm/yr. Rounded to the 3rd decimal. |
| SRMax | Float | mm/yr | Maximum value of the slip rate in mm/yr. Rounded to the 3rd decimal. |
| SRAMean | Float | mm/yr | Aritmetic mean value of the slip rate in mm/yr. Rounded to the 3rd decimal. |
| SRGMean | Float | mm/yr | Geometric mean value of the slip rate in mm/yr. Rounded to the 3rd decimal. |
| Complex | Float | scalar | Index between 0-1 that indicates the level of complexity of the fault geometry. Rounded to the 4th decimal. |
| TopoAvg | Float | m | Average topographic elevation above the fault trace, positive upward from sea level. Rounded to the nearest integer. |
| MohoAvg | Float | km | Value of the average Moho depth below the fault trace, positive downward from sea level. Rounded to the half kilometer. |
| Mu | Float | GPa | Average shear modulus or rigidity. Fixed for coherence with fault scaling relations used to estimate maximum magnitude. |
| FaultType | Char(2) | n.a. | One-letter or two-letter code: R = reverse, N = normal, RL = right-lateral transcurrent, LL = left-lateral transcurrent. |
| FSLTecto | Char(3) | n.a. | Three-letter code: MAR = Mid-Atlantic Ridge; INT = interplate region; SCR = stable continental region. |
| FSLName | Char(24) | n.a. | Leonard2014_Interplate or Leonard2014_SCR |
| FSLSlip | Char(2) | n.a. | Two-letter code: DS = dip slip; SS = strike slip. |
| FSLDim | Char(1) | n.a. | One-letter code indicating which rupture dimension is used to estimate the maximum magnitude: L = length, W = width, A = area, D = displacement. |
| MwMaxP02 | Float | scalar | Value of 2nd percentile of the maximum moment magnitude distribution. Rounded to the 2nd decimal. |
| MwMaxP05 | Float | scalar | Value of 5th percentile of the maximum moment magnitude distribution. Rounded to the 2nd decimal. |
| MwMaxAvg | Float | scalar | Mean value of the maximum moment magnitude distribution. Rounded to the 2nd decimal. |
| MwMaxP95 | Float | scalar | Value of 95th percentile of the maximum moment magnitude distribution. Rounded to the 2nd decimal. |
| MwMaxP98 | Float | scalar | Value of 98th percentile of the maximum moment magnitude distribution. Rounded to the 2nd decimal. |
| M0RMin | Float | Nm | Minimum value of the moment rate of the fault. Logarithmic, base 10, value rounded to the 4th decimal. |
| M0RMax | Float | Nm | Maximum value of the moment rate of the fault. Logarithmic, base 10, value rounded to the 4th decimal. |

| | | | |
|---|---|---|---|
| M0RAMean | Float | Nm | Arithmetic mean of the moment rate of the fault. Logarithmic, base 10, value rounded to the 4th decimal. |
| M0RGMean | Float | Nm | Geometric mean of the moment rate of the fault. Logarithmic, base 10, value rounded to the 4th decimal. |

**Table A4 Definition of the crustal fault attributes for the EFSM20_CFDepths files.**

| Field | Variable | Units | Description |
|---|---|---|---|
| IDFS | Char(7) | n.a. | Identifier of the fault source within EFSM20 |
| IDDS | Char(3) | n.a. | Number of the dataset linked to the file "DescriptionOfDatasets". |
| IDSource | Char(24) | n.a. | Identifier given in the original source, if available. |
| IDContour | Integer | n.a. | Ordinal that identifies the number of the depth isoline within each crustal fault source. |
| Depth | Float | km | Depth value of the isoline, positive downward from sea level. The isoline spacing is fixed at 0.5 km depth. The top and bottom lines of the fault plane are included. |

**Table A5 Attributes of the slab depths.**

| Field | Variable | Units | Description |
|---|---|---|---|
| IDFS | Char(7) | n.a. | Identifier of the fault source within EFSM20 |
| SlabName | Char(24) | n.a. | Long name of the subduction system (Gibraltar Arc, Calabrian Arc, Hellenic Arc, Cyprus Arc). |
| ShortName | Char(3) | n.a. | Short name of the subduction system (GiA, CaA, HeA, CyA). |
| IDDS | Char (3) | n.a. | Number of the dataset linked to the file "DescriptionOfDatasets". |
| IDSource | Char(24) | n.a. | Identifier given in the original source |
| IDContour | Char (5) | n.a. | Identifier of the individual depth isoline coded as follow: three-letter code of the model name, followed by an ordinal including leading zeroes. |
| Depth | Float | km | Depth value of the isoline, positive downward from sea level. The isoline spacing is fixed at 1 km up to 40 km depth, and at 10 km below. The deepest slab isoline is fixed at 300 km depth. |

995    **Table A6 Attributes of the subduction interface. Geometry and behavior parameters.**

| Field | Variable | Units | Description |
|---|---|---|---|
| IDFS | Char(7) | n.a. | Identifier of the fault source within EFSM20. |
| SlabName | Char(24) | n.a. | Long name of the subduction system (Gibraltar Arc, Calabrian Arc, Hellenic Arc, Cyprus Arc). |

| ShortName | Char(3) | n.a. | Short name of the subduction system (GiA, CaA, HeA, CyA). |
|---|---|---|---|
| IDDS | Char(3) | n.a. | Number of the dataset linked to the file "DescriptionOfDatasets". |
| IDSource | Char(24) | n.a. | Identifier given in the original source |
| USD1 | Float | km | Value of the minimum upper seismogenic depth of the subduction interface, positive downward from sea level. Rounded to the nearest integer. |
| USD2 | Float | km | Value of the intermediate upper seismogenic depth of the subduction interface, positive downward from sea level. Rounded to the nearest integer. |
| USD3 | Float | km | Value of the maximum upper seismogenic depth of the subduction interface, positive downward from sea level. Rounded to the nearest integer. |
| LSD1 | Float | km | Value of the minimum lower seismogenic depth of the subduction interface, positive downward from sea level. Rounded to the nearest integer. |
| LSD2 | Float | km | Value of the intermediate lower seismogenic depth of the subduction interface, positive downward from sea level. Rounded to the nearest integer. |
| LSD3 | Float | km | Value of the maximum lower seismogenic depth of the subduction interface, positive downward from sea level. Rounded to the nearest integer. |
| ConvRate1 | Float | mm/yr | Value of the lowest estimate of the convergence rate. Rounded to the 2nd decimal. |
| ConvRate2 | Float | mm/yr | Value of the average estimate of the convergence rate. Rounded to the 2nd decimal. |
| ConvRate3 | Float | mm/yr | Value of the highest estimate of the convergence rate. Rounded to the 2nd decimal. |
| ConvAz1 | Float | degrees | Lowest azimuth value of the upper-plate and lower-plate convergence direction between 0-180° increasing clockwise from the North. Rounded to the nearest integer. |
| ConvAz2 | Float | degrees | Average azimuth value of the upper-plate and lower-plate convergence direction between 0-180° increasing clockwise from the North. Rounded to the nearest integer. |
| ConvAz3 | Float | degrees | Highest azimuth value of the upper-plate and lower-plate convergence direction between 0-180° increasing clockwise from the North. Rounded to the nearest integer. |
| TopoMin | Float | km | Minimum topobathymetric elevation above the subduction interface area. Rounded to the 1st decimal. |
| TopoAvg | Float | km | Average topobathymetric elevation above the subduction interface area. Rounded to the 1st decimal. |
| TopoMax | Float | km | Maximum topobathymetric elevation above the subduction interface area. Rounded to the 1st decimal. |
| MohoMin | Float | km | Value of the minimum Moho depth below the subduction interface, positive downward from sea level, as measured in the shallowest region of the subduction interface. Rounded to the nearest integer. |
| MohoAvg | Float | km | Value of the average Moho depth below the subduction interface, positive downward from sea level, as measured in the shallowest region of the subduction interface. Rounded to the nearest integer. |
| MohoMax | Float | km | Value of the maximum Moho depth below the subduction interface, positive downward from sea level, as measured in the shallowest region of the subduction interface. Rounded to the nearest integer. |
| LengthMin | Float | km | Length of the shortest depth isoline within the subduction interface. Rounded to the nearest integer. |

| | | | |
|---|---|---|---|
| LengthAvg | Float | km | Average length of all depth isolines within the subduction interface. Rounded to the nearest integer. |
| LengthMax | Float | km | Length of the longest depth isoline within the subduction interface. Rounded to the nearest integer. |
| AreaInMap | Float | sq km | Total area occupied by the vertical projection onto the ground surface of the subduction interface. |
| AreaDD | Float | sq km | Total area of the slab-interface dipping surface, comprised between the uppermost and lowermost depths. Rounded to the nearest integer. |
| WidthAvg | Float | km | Average width of the slab-interface surface measured along the dip-direction (orthogonal to strike). Rounded to the nearest integer. |
| DipAvg | Float | degrees | Average dip angle (slope) of the slab-interface surface measured along the dip-direction (orthogonal to strike). Rounded to the nearest integer. |

**Table A7 Attributes of the subduction interface discretization.**

| Field | Variable | Units | Description |
|---|---|---|---|
| IDFS | Char(7) | n.a. | Identifier of the fault source within EFSM20. |
| SlabName | Char(24) | n.a. | Long name of the subduction system (Gibraltar Arc, Calabrian Arc, Hellenic Arc, Cyprus Arc). |
| ShortName | Char(3) | n.a. | Short name of the subduction system (GiA, CaA, HeA, CyA). |
| IDDS | Char(3) | n.a. | Number of the dataset linked to the file "DescriptionOfDatasets". |
| IDSource | Char(24) | n.a. | Identifier given in the original source |
| IDInterval | Char (5) | n.a. | Identifier of the individual depth interval coded as follow: three-letter code of the model name, followed by an ordinal including leading zeroes. |
| DepthHi | Float | km | Value of the upper seismogenic depth of the subduction interface, positive downward from sea level. Rounded to the nearest integer. |
| DepthLo | Float | km | Value of the lower seismogenic depth of the subduction interface, positive downward from sea level. Rounded to the nearest integer. |
| LengthHi | Float | km | Length of the upper isoline of the depth interval. Rounded to the nearest integer. |
| LengthLo | Float | km | Length of the lower isoline of the depth interval. Rounded to the nearest integer. |
| LengthAvg | Float | km | Average length of the upper and lower isolines of the depth interval. Rounded to the nearest integer. |
| AreaInMap | Float | sq km | Total area occupied by the vertical projection onto the ground surface of the subduction interface. |
| AreaDD | Float | sq km | Total area of the slab-interface dipping surface, comprised between the uppermost and lowermost depths. Rounded to the nearest integer. |
| WidthAvg | Float | km | Average width of the slab-interface surface measured along the dip-direction (orthogonal to strike). Rounded to the nearest integer. |

| | | | |
|---|---|---|---|
| DipAvg | Float | degrees | Average dip angle (slope) of the slab-interface surface measured along the dip-direction (orthogonal to strike). Rounded to the nearest integer. |
| TopoMin | Float | m | Minimum topo-bathymetric elevation above the subduction interface area. Rounded to the 1st decimal. |
| TopoAvg | Float | m | Average topo-bathymetric elevation above the subduction interface area. Rounded to the 1st decimal. |
| TopoMax | Float | m | Maximum topo-bathymetric elevation above the subduction interface area. Rounded to the 1st decimal. |
| MuPREM | Float | GPa | Shear modulus (or rigidity) at the depth interval of the slab discretization, as derived from Dziewonski and Anderson (1981). Rounded to the nearest integer. |
| MuSC19 | Float | GPa | Shear modulus (or rigidity) at the depth interval of the slab discretization, as derived from Scala et al. (2019). Rounded to the nearest integer. |
| MuBL99 | Float | GPa | Shear modulus (or rigidity) at the depth interval of the slab discretization, as derived from Bilek and Lay (1999). Rounded to the nearest integer. |
| MuSR19Min | Float | GPa | Shear modulus (or rigidity), - 1 standard deviation, at the depth interval of the slab discretization, as derived from Sallarèr and Ranero (2019). Rounded to the nearest integer. |
| MuSR19Avg | Float | GPa | Shear modulus (or rigidity) at the depth interval of the slab discretization, as derived from Sallarèr and Ranero (2019). Rounded to the nearest integer. |
| MuSR19Max | Float | GPa | Shear modulus (or rigidity), + 1 standard deviation, at the depth interval of the slab discretization as derived from Sallarèr and Ranero (2019). Rounded to the nearest integer. |

**Table A8 Attributes of the subduction interface realizations.**

| Field | Variable | Units | Description |
|---|---|---|---|
| IDFS | Char(7) | n.a. | Identifier of the fault source within EFSM20. |
| SlabName | Char(24) | n.a. | Long name of the subduction system (Gibraltar Arc, Calabrian Arc, Hellenic Arc, Cyprus Arc). |
| ShortName | Char(3) | n.a. | Short name of the subduction system (GiA, CaA, HeA, CyA). |
| ModelCode | Char(5) | n.a. | Five-character code formed by the ShortName string followed by two numbers (1-2-3) representing the combination of the USD and LSD values. This code also identifies a different polygon in the map, corresponding to the subduction interface area enclosed between the two different depth isolines. |
| USD | Float | km | Value of the upper seismogenic depth of the subduction interface, positive downward from sea level. Rounded to the nearest integer. |
| LSD | Float | km | Value of the lower seismogenic depth of the subduction interface, positive downward from sea level. Rounded to the nearest integer. |
| TotalArea | Float | sq km | Value of the subduction interface area of the model realization. Rounded to the nearest integer. |
| Mu1 | Float | GPa | Shear modulus (or rigidity) based on the depth range of the subduction interface realization (weighted average of the expected values -1 s.d.). Rounded to the nearest integer. |

| | | | |
|---|---|---|---|
| Mu2 | Float | GPa | Shear modulus (or rigidity) based on the depth range of the subduction interface realization (weighted average of the expected values). Rounded to the nearest integer. |
| Mu3 | Float | GPa | Shear modulus (or rigidity) based on the depth range of the subduction interface realization (weighted average of the expected values +1 s.d.). Rounded to the nearest integer. |
| ConvRate1 | Float | mm/yr | Value of the lowest estimate of the convergence rate. Rounded to the 2nd decimal. |
| ConvRate2 | Float | mm/yr | Value of the average estimate of the convergence rate. Rounded to the 2nd decimal. |
| ConvRate3 | Float | mm/yr | Value of the highest estimate of the convergence rate. Rounded to the 2nd decimal. |
| MwMax1 | Float | scalar | Maximum moment magnitude based on the total area of the subduction interface realization (expected value -1s). Rounded to the 2nd decimal. |
| MwMax2 | Float | scalar | Maximum moment magnitude based on the total area of the subduction interface realization (expected value). Rounded to the 2nd decimal. |
| MwMax3 | Float | scalar | Maximum moment magnitude based on the total area of the subduction interface realization (expected value +1s). Rounded to the 2nd decimal. |
| TM0Rate11 | Float | Nm | Moment rate of the subduction interface realization obtained from the product of TotalArea*Mu1*ConvRate1. Logarithmic, base 10, value rounded to the 3rd decimal. |
| TM0Rate12 | Float | Nm | Moment rate of the subduction interface realization obtained from the product of TotalArea*Mu1*ConvRate2. Logarithmic, base 10, value rounded to the 3rd decimal. |
| TM0Rate13 | Float | Nm | Moment rate of the subduction interface realization obtained from the product of TotalArea*Mu1*ConvRate3. Logarithmic, base 10, value rounded to the 3rd decimal. |
| TM0Rate21 | Float | Nm | Moment rate of the subduction interface realization obtained from the product of TotalArea*Mu2*ConvRate1. Logarithmic, base 10, value rounded to the 3rd decimal. |
| TM0Rate22 | Float | Nm | Moment rate of the subduction interface realization obtained from the product of TotalArea*Mu2*ConvRate2. Logarithmic, base 10, value rounded to the 3rd decimal. |
| TM0Rate23 | Float | Nm | Moment rate of the subduction interface realization obtained from the product of TotalArea*Mu2*ConvRate3. Logarithmic, base 10, value rounded to the 3rd decimal. |
| TM0Rate31 | Float | Nm | Moment rate of the subduction interface realization obtained from the product of TotalArea*Mu3*ConvRate1. Logarithmic, base 10, value rounded to the 3rd decimal. |
| TM0Rate32 | Float | Nm | Moment rate of the subduction interface realization obtained from the product of TotalArea*Mu3*ConvRate2. Logarithmic, base 10, value rounded to the 3rd decimal. |
| TM0Rate33 | Float | Nm | Moment rate of the subduction interface realization obtained from the product of TotalArea*Mu3*ConvRate3. Logarithmic, base 10, value rounded to the 3rd decimal. |

**Table A9 Attributes of the intraslab geometric parameters.**

| Field | Variable | Units | Description |
|---|---|---|---|
| IDFS | Char(7) | n.a. | Identifier of the fault source within EFSM20. |
| SlabName | Char(24) | n.a. | Long name of the subduction system (Gibraltar Arc, Calabrian Arc, Hellenic Arc, Cyprus Arc). |
| ShortName | Char(3) | n.a. | Short name of the subduction system (GiA, CaA, HeA, CyA). |

| IDDS | Char(3) | n.a. | Number of the dataset linked to the file "DescriptionOfDatasets". |
|------|---------|------|------------------------------------------------------------------|
| IDNode | Char(8) | n.a. | Identifier of the individual nodes coded as follows: three-letter code of the model name, followed by an ordinal including leading zeroes. |
| Lon | Float | degrees | Longitude of the node in decimal degrees, positive eastward, datum WGS84 (EPSG 4326). The east-west spacing between nodes is fixed at 10 km. |
| Lat | Float | degrees | Latitude of the node in decimal degrees, positive northward, datum WGS84 (EPSG 4326). The north-south spacing between nodes is fixed at 10 km. |
| Depth | Float | km | Depth of the node, positive downward from sea level. The node depth spacing is fixed at 10 km, starting from 5 km. |
| Strike | Float | degrees | Value of the slab orientation, between 0-360° increasing clockwise from the north following the right-hand rule. Recalculated from the nearest point on the slab mid-surface. Rounded to the nearest integer. |
| DipDir | Float | degrees | Value of the slab dip direction (downward direction of maximum slope), between 0-360° increasing clockwise from the north. Calculated as strike + 90°. Rounded to the nearest integer. |
| Dip | Float | degrees | Value of the slab dip angle, between 0-90° increasing downward from the horizontal. Recalculated from the nearest point on the slab mid-surface. Rounded to the nearest integer. |

1000

## Appendix B

Large version of the maps shown in Figure 5 in the main text (the color classes used in these figures are the same as those distributed by OGC WMS web services).
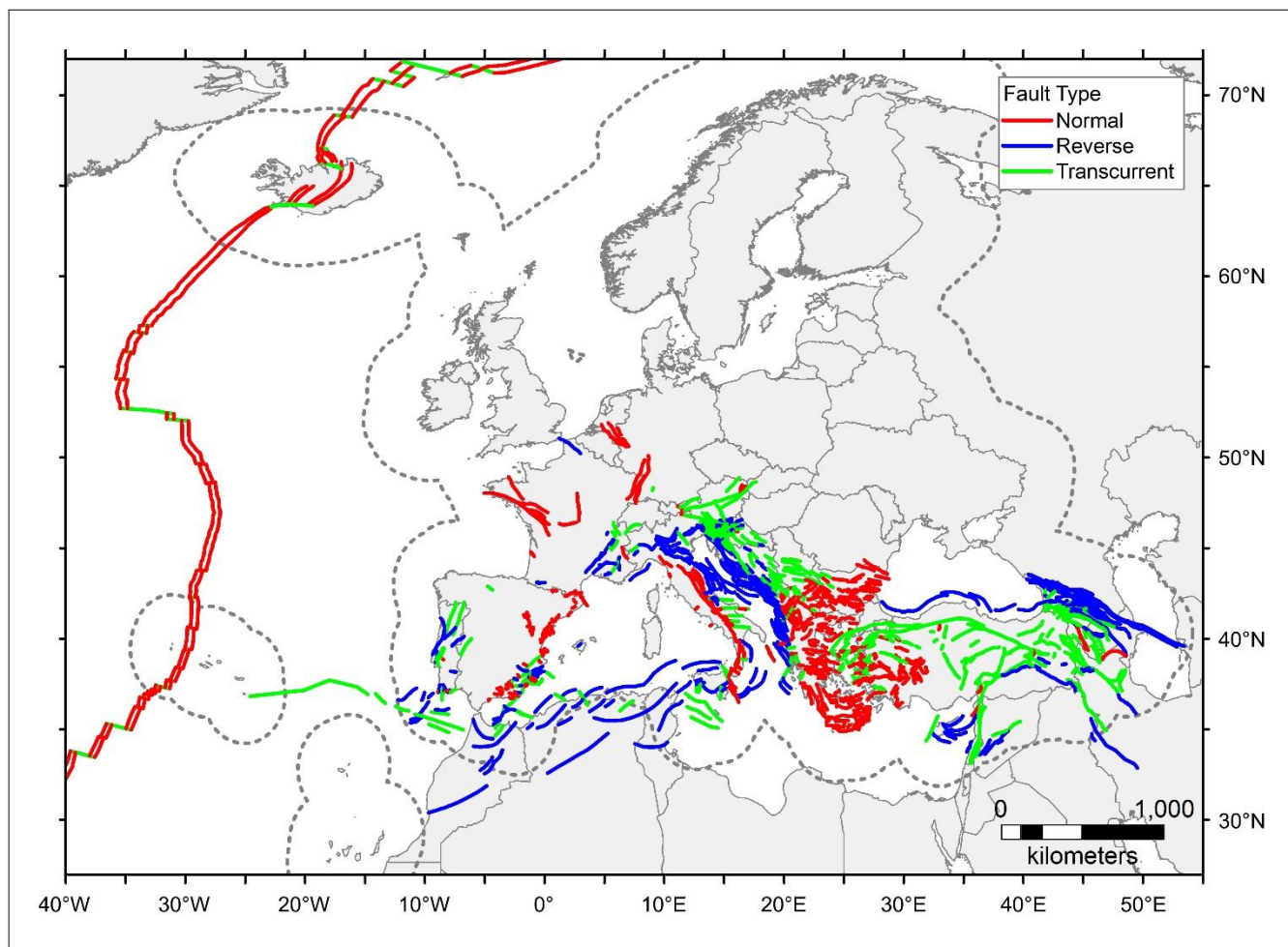
1005    **Figure B1: EFSM20 crustal faults color-coded according to faulting type.**
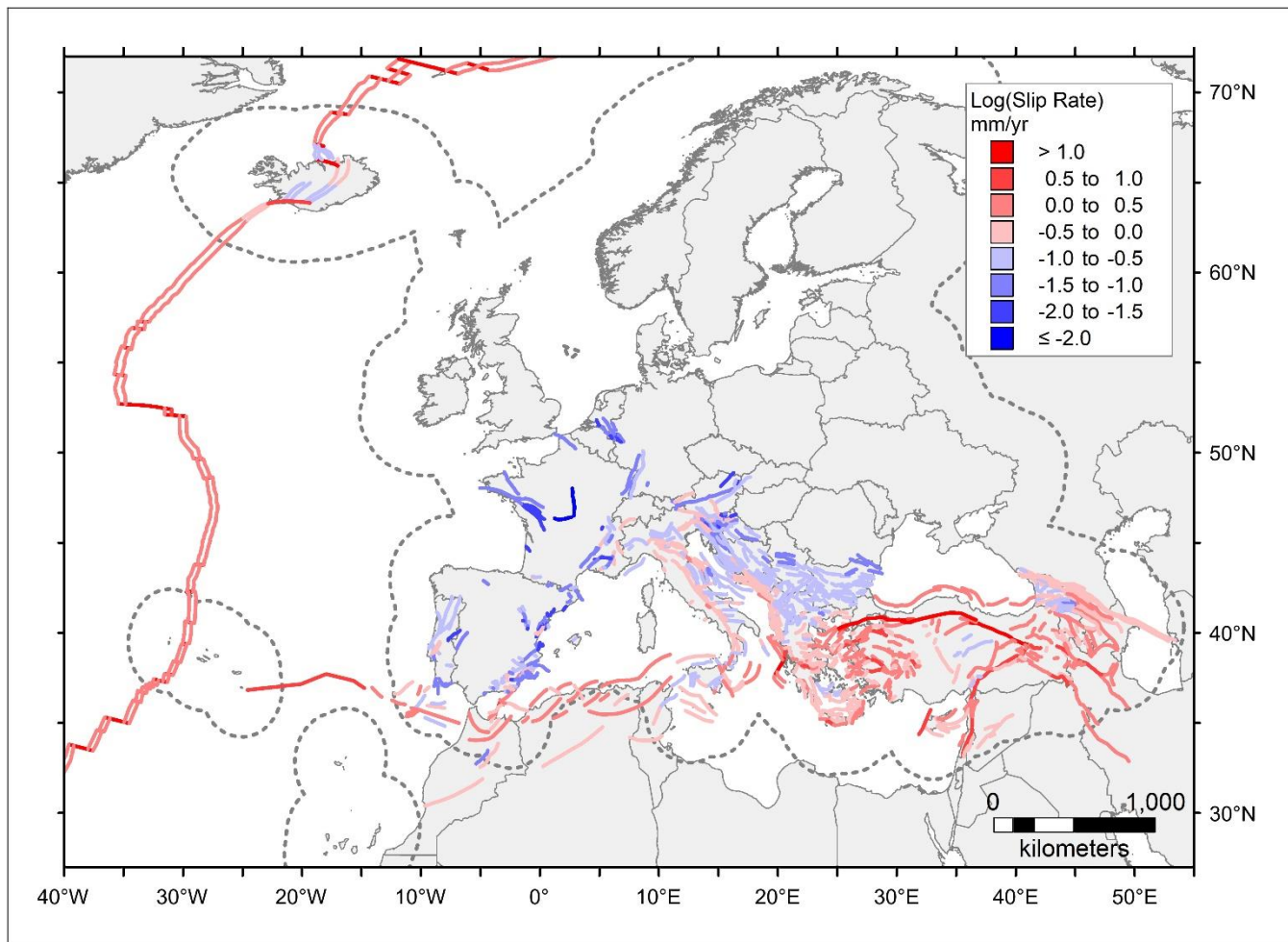
**Figure B2: EFSM20 crustal faults color-coded according to average slip rate.**
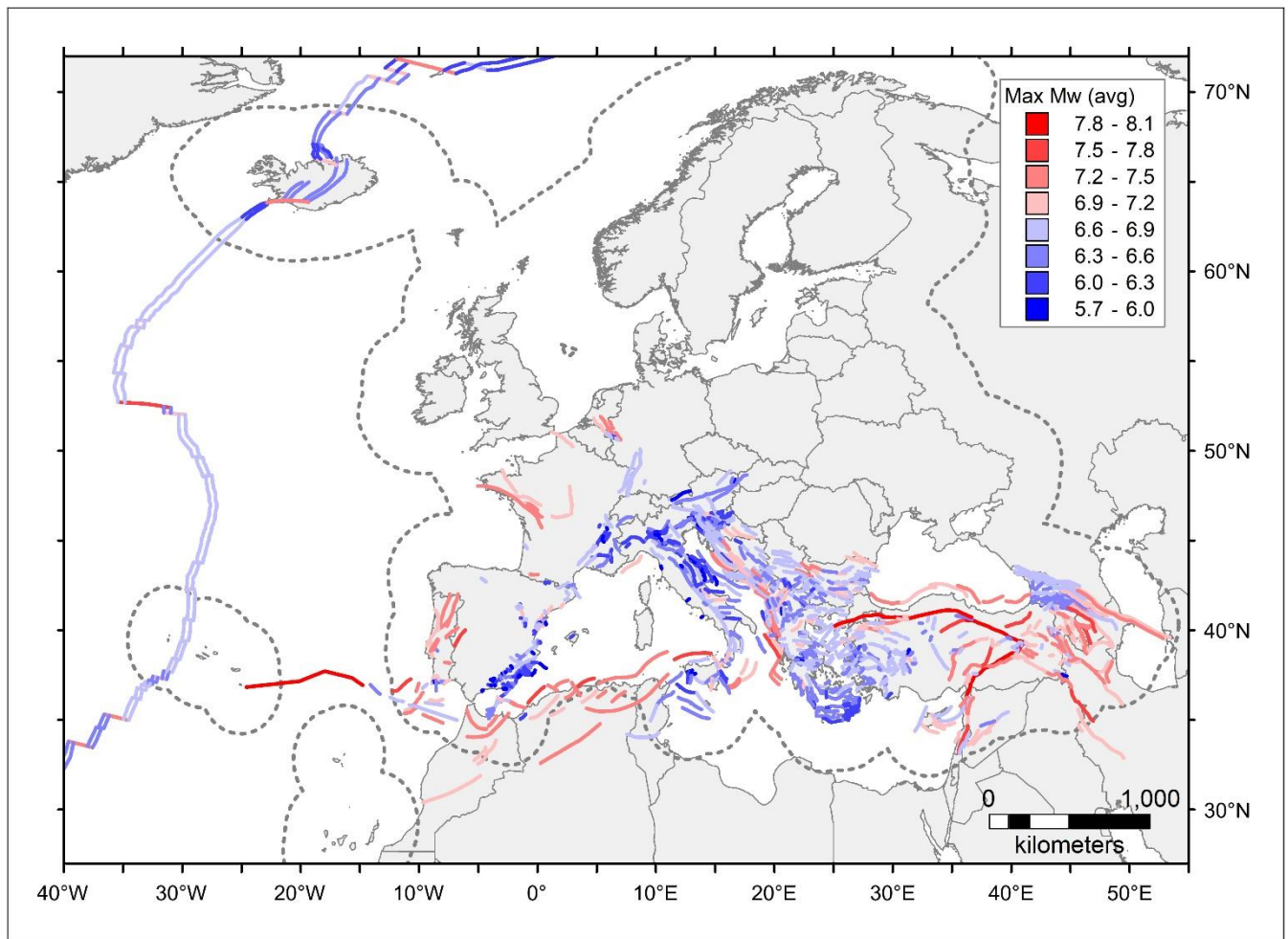
**Figure B3: EFSM20 crustal faults color-coded according to maximum moment magnitude.**
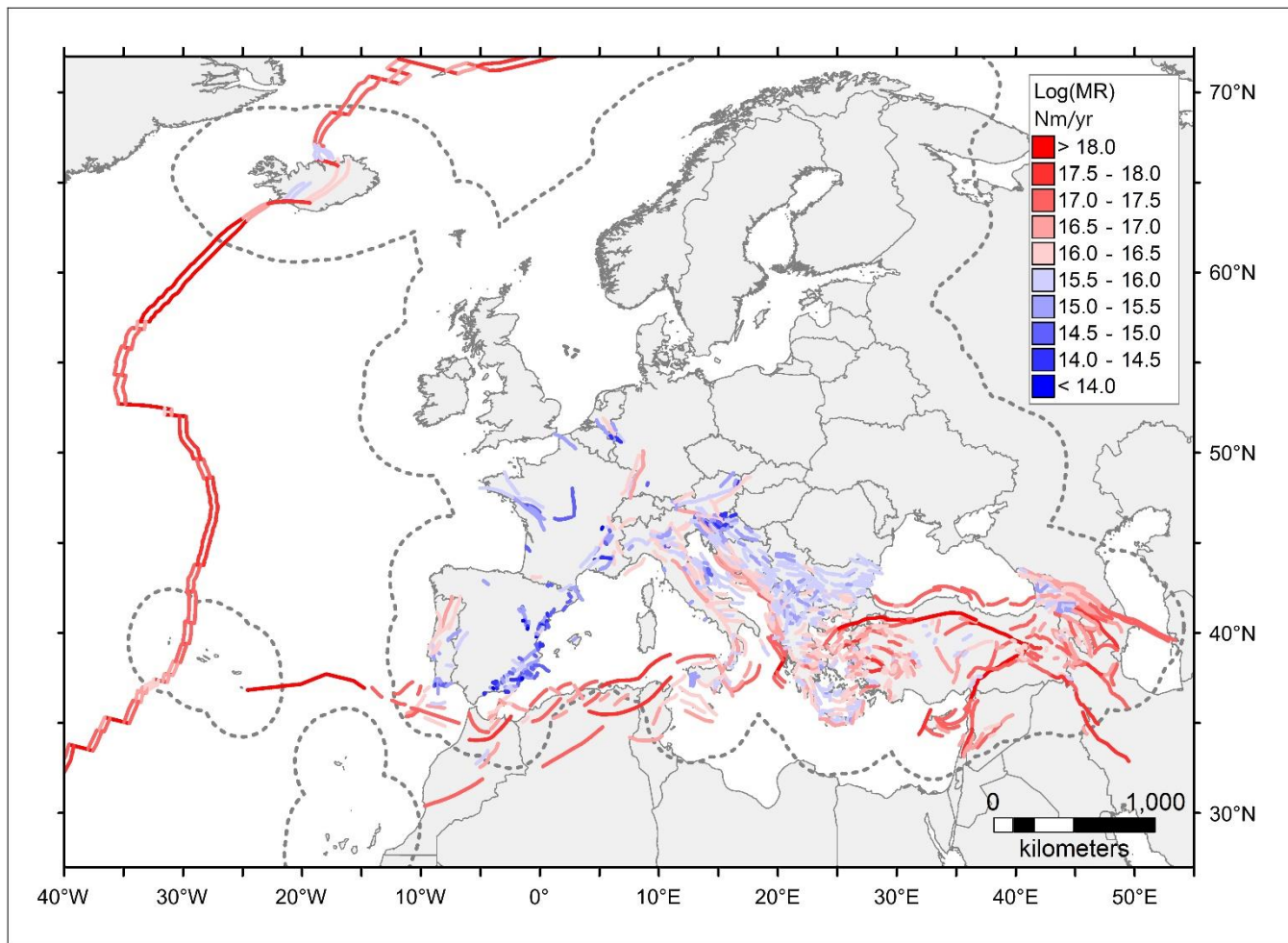
1010

**Figure B4: EFSM20 crustal faults color-coded according to average moment rate.**